SANDIA REPORT
SAND2024-13381
UUR
Printed October 2024

Sandia National Laboratories

Methane Integrated Monitoring and Measurement System Design

Jake P. Zenker, Lekha Patel, Anneliese Lilje, Philip R. Miller, Joshua Whiting, Jennifer Lewis, Daniel Krofcheck, Kurtis Shuler, Clare Amann, Andrew Glen

Controlled by: Sandia National Laboratories/Lekha Patel

Prepared by
Sandia National Laboratories
Albuquerque, New Mexico
87185 and Livermore,
California 94550

Issued by Sandia National Laboratories, operated for the United States Department of Energy by National Technology & Engineering Solutions of Sandia, LLC.

ABSTRACT

Methane (CH_4), an abundant greenhouse gas, is the second largest contributor to global warming after carbon dioxide (CO_2). In comparison to CO_2, CH_4 has a larger warming effect over a much shorter lifetime. While technologies to radically reduce global carbon dioxide emissions are materializing, rapid reductions in methane emissions are needed to limit near-term warming. Methane is primarily emitted as a byproduct from agricultural activities and energy extraction/utilization and is currently monitored via bottom-up (i.e., activity level) or top-down (via airborne or satellite retrievals) approaches. However, significant methane leaks remain undetected, and emission rates are challenging to characterize with current monitoring frameworks. In this report, we study methane leaks from oil and gas infrastructure using a tiered monitoring approach that combines bottom-up and top-down approaches in an integrated framework. We describe the individual advantages of bottom-up and top-down sensors in both stationary and mobile settings before characterizing how a fully integrated framework can improve predictions and uncertainties of potential leak locations and their emission rates. Further, we study the impact of different atmospheric (wind) conditions on integrated methane monitoring and develop a probabilistic approach to optimal sensor placement, thereby shortening detection times and improving monitoring capabilities. Last, we discuss how biogenic flux modeling can be used to improve assessment of background methane concentrations needed to fully assess the sensitivity of a tiered monitoring system.

ACKNOWLEDGEMENTS

We would first like to acknowledge Mark Ackermann for useful discussions and his subject matter expertise on existing satellite instrumentation for monitoring. We would also like to thank Ben Cook and Erik Webb for their ongoing programmatic support, and DOE's Fossil Energy Carbon Management (FECM) program for funding this work.

CONTENTS

LIST OF FIGURES

LIST OF TABLES

This page left blank

EXECUTIVE SUMMARY

This report studies multi-sensor monitoring of methane emissions as a preliminary step to demonstrating the power of a multi-tier framework (i.e., one which integrates measurements of sensors placed at varying spatial-temporal scales) in methane monitoring. We define three tier levels: Tier 1 indicates monitoring across large spatial areas (e.g., country level) that may include airborne instruments such as satellites. Tier 2 indicates monitoring across smaller spatial areas (e.g., county level) with higher accuracy/resolution that may include sensors placed on drones, airplanes, or towers. Tier 3 indicates monitoring at single-emission site levels that may include ground-based point sensors deployable at fixed locations or on mobile instrumented platforms. In doing so, we capture monitoring benefits and challenges with single tiered sensors, including extensive lists of off-the-shelf instruments that could be considered for monitoring at each tier.

To study an integrated methane framework, combining sensors from each tier for optimal monitoring, we chose the Permian Basin as our exemplar, in which a significant portion of the United States' oil and gas infrastructure is situated. To enable modeling of methane leaks from potential emission sources within such an area, we first define a Gaussian Plume model with the ability to capture methane plumes which will be used to represent leaks. Using this model, zones of detection, defined as radii around emission sources in which leaks can be detected, are studied at varying altitudes, wind speeds, and emission rates (above background) using sensors located in both Tier 2 and Tier 3. By visualizing emission sources in the Permian Basin around roads on which mobile sensors could be deployed, we can quantify the number of emission sources monitorable using Tier 2 and Tier 3 sensors and determine the potential for mobile monitoring in the Permian. Given this, we utilize Sandia developed Chama software for optimal sensor placement of Tier 2-3 sensors, including stationary and mobile sensors, on two areas of the Permian where roads intersect with oil and gas operations.

Camera based mobile sensors are somewhat challenging to model within Chama's setup; however, we demonstrate the ability to optimize sensor placement based on budget and cost to maximize monitoring capabilities and detectability of leaks from various Tier 3 sensor options, which may include mobile deployment. Using Chama's output, we subsequently formulate an integrated (Tiers 1-3) methane monitoring network which we show to provide greater methane concentration data than using a single

tier alone. Using the tiered network, we formulate a statistical model capable of learning source attribution (i.e., underlying emission rates from leaks) with quantifiable uncertainties, and show that a fully tiered system improves predictive accuracy with reduced uncertainties compared with Tiers 2-3 or Tier 3 networks alone. We additionally use an inverse Gaussian Plume model to study source attribution as sensor sensitivities, sensor density and standoff distances are varied, which may help determine specific sensors that could be utilized as part of an integrated system. In doing so, we are able to provide cost estimates based upon monitoring accuracy and detection times for integrated methane monitoring in the Permian. Last, we discuss biogenic methane modeling as an important area of future work in order to accurately determine background methane concentrations, to improve modeling of continuous methane emissions from natural sources such as from agriculture and permafrost, and to drive down uncertainties associated with non-oil and gas sources.

ACRONYMS AND TERMS

Acronym/Term	Definition
AERMOD	Air Quality Dispersion Modeling
CONOPS	Concept of Operations
FAA	Federal Aviation Administration
GHG	Greenhouse gas
GWP	Global Warming Potential
IPCC	Intergovernmental Panel on Climate Change
QGIS	Quantum Geographic Information System
UAV	Unmanned Aerial Vehicles
UNFCCC	United Nations Framework Convention on Climate Change
ZOD	Zone of Detection
ZODB	Zone of Detection Buffer

1. INTRODUCTION

Long-lived atmospheric pollutants, especially from fossil fuel burning, have long been known to have a lasting impact on (positive) global radiative forcing or *warming.*[1] Two of particular concern are carbon dioxide, persisting for thousands of years in the atmosphere and methane, which remains for at most a decade.[2] Despite its short lifetime, methane increases short-term peak warming due to its higher Global Warming Potential (25-35 times greater than carbon dioxide) and is estimated to account for 30% of global temperature increase since industrialization.[3] Aggregated forcing effects between different gases are causing global temperatures to rise at unprecedented rates and the resulting detrimental impacts, ranging from increased droughts, more severe storms, hotter temperatures, warming oceans, and increased health risks[4] are becoming irreversible.

However, the IPCC has determined future warming greater than 1.5°C above pre-industrial levels is **not** unavoidable, but rather depends on continued rates of emission. In particular, the IPCC's previous recommendation to reduce anthropogenic methane emissions to limit global temperature rise beyond 1.5°C by 2030 was inspired by new evidence at the time which showed a larger methane forcing[5] than previously determined. Due to its short-term lifespan, eliminating or severely cutting methane emissions is estimated to result in both immediate cooling,[6] and prevention of catastrophic short-term climate effects, particularly as longer-term technologies to reduce CO_2 emissions are being actively developed. Consequently, following the 2015 Paris Agreement, many countries have pledged to reduce their total greenhouse gas emissions, with methane being singled-out via the 2021 Global Methane Pledge,[7] aiming to reduce methane emissions by at least 30% below 2020 levels by 2030. A huge challenge with the Global Methane Pledge, however, is the lack of complete global support, particularly from countries with high methane emissions, as illustrated by the 1.8% increase in emissions in 2022, due primarily to industrialization.

While country-level commitments are becoming increasingly important and necessary, low-cost opportunities to curb methane emissions remain largely under deployed. The largest sources of anthropogenic methane emissions are reported to be from agriculture and energy production. However, the data used to report the emissions levels varies greatly, and emphasizes the global need to improve emission quantifications from various sources.

For example, oil and gas (O&G) operations are documented as the largest *industrial* source of anthropogenic methane emissions in the United States, with the International Energy Agency (IEA) estimating a potential to reduce around 70% of global methane emissions from O&G facilities with existing technologies.[7] Unintentional methane emissions occur as *leaks* across all levels of the extractive industry and O&G pipeline, with major sources emerging from production, processing, storage, and distribution. Specific limitations in gathering, processing, and transportation infrastructure lead to significant venting and excess flaring of both carbon dioxide and methane.

At approximately 37%, agriculture is reported to be the largest source of anthropogenic methane emissions globally, with new ideologies pushing farmers to move towards more sustainable feed additives and higher plant than livestock food production. Methane emissions produced from agricultural waste at landfills are additionally becoming increasingly capturable with state-of-the-art technologies. When coupled with global food security, naturally occurring methane emissions such as those from biogenic sources (e.g., livestock and agriculture) may be harder to limit than those from O&G facilities, yet they importantly aggregate to form *background* methane rates beyond which it becomes necessary for novel methodologies and technologies to discern methane levels from industrial facilities.

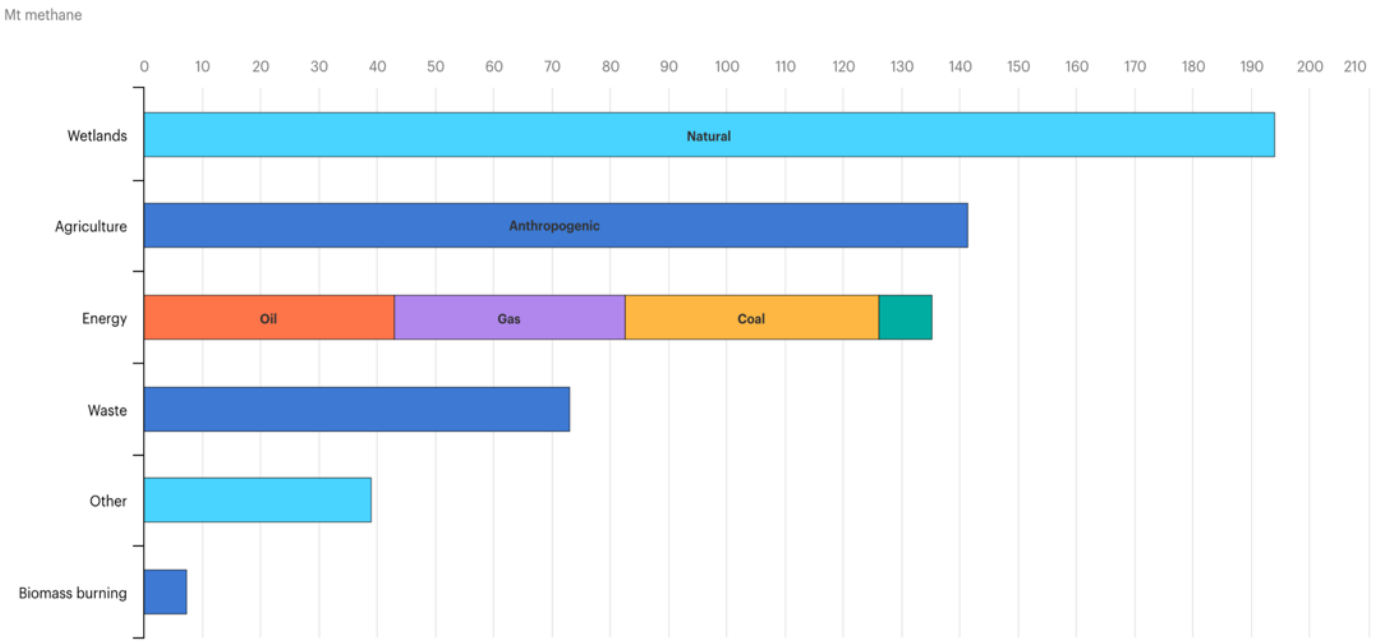

Figure 1: Energy sector emissions are from the Global Methane Tracker for 2021; non-energy sector emissions are the average of estimates available from UNFCCC, CAIT, EDGAR and CEDS for 2018 or 2019. Natural sources and biomass burning are top-down median estimates and bottom-up median estimates respectively from the Global Methane Budget for 2017.[8]

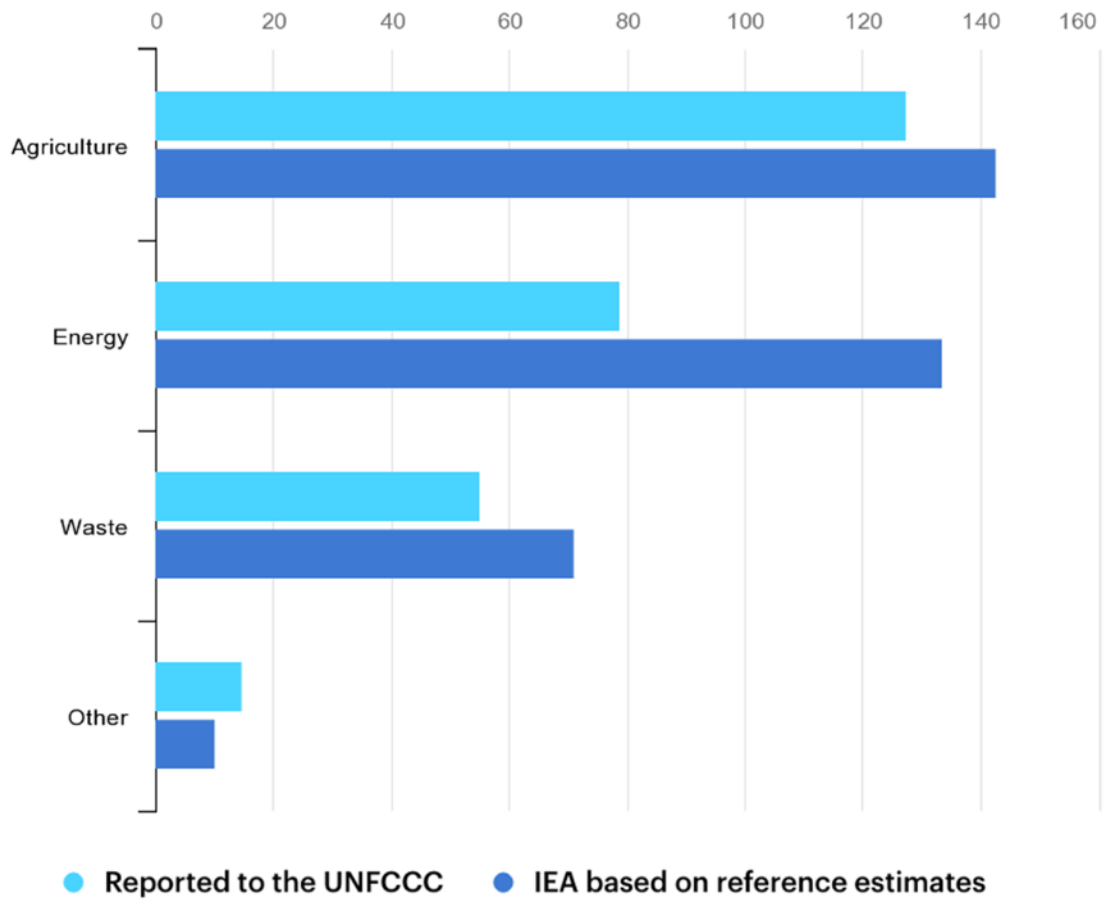

Figure 2: UNFCCC submissions from the Greenhouse Gas Data Interface for the latest year available (Mt methane). Reference estimates for energy are the Methane Tracker estimates for 2022. For non-energy sector emissions, these are taken as an average of estimates available for 2019, 2020, or 2021 from UNFCCC, CAIT, EDGAR and CEDS (see Methodology for further information).

There is therefore an urgent need for more accurate data to establish both baseline methane levels and to determine rates of emissions of anthropogenic operations. Accurate detection of leaks from normal operations as well as abnormal emissions from infrastructure failure will be required to assess the success of mitigation techniques.

This report proposes a strategy to optimize and evaluate the performance of monitoring networks that can be deployed on a regional scale to detect and quantify methane emissions from oil and gas production operations.

1.1. A Multi-Tiered Approach to Methane Leak Detection

There are several different types (or tiers) of platforms that can be used to monitor methane concentrations and emissions. For this analysis, we crudely define these tiers to be Satellite (Tier 1), Aerial (Tier 2), or Ground (Tier 3) platforms.

Each of these Tiers has advantages and disadvantages. Satellite platforms, for instance, can sense methane across large swaths of the Earth's atmosphere. However, the sensitivity, accuracy, and spatial resolution of most of these systems are insufficient for the detection of individual leaks. While advanced satellite platforms, such as the new Carbon Mapper satellite, have demonstrated their ability to detect large individual sources (e.g., super emitters) with improved spatial resolution and sensitivity, their revisit time, which may be several days or weeks, is too long since most methane emission events associated with oil and gas operations are typically an hour or less in duration. Aerial sensors provide robust spatial coverage, albeit much less than satellites, and are adequately sensitive and accurate enough to detect and quantify emissions from individual sources. However, these platforms are cost and labor intensive and therefore cannot be used as a means for continuous monitoring. Ground-based sensors, which may be stationary or mobile, have the highest level of sensitivity and accuracy amongst all the tiers and can continuously monitor methane concentrations. However, because their footprint is small, a vast network of these sensors is required to perform source attribution; the cost of such a network may be prohibitively expensive.

Due to the large variety of sensor types, spatial coverages, and methane sources, understanding the full potential of an integrated methane platform is a challenging task. To this end, we focus on developing an optimization strategy for an integrated approach from O&G methane sources in the Permian Basin. By combining a range of sensors across all tiers, with quantifiable limits of detection, we subsequently showcase the power of a fully integrated system in accurately covering concentration fields and performing the inverse source attribution procedure: utilizing a statistical framework to spatially identify leak sources and their emission rates with quantifiable uncertainties. In doing so, we can determine methane leak rates and concentrations at lower uncertainties than what is achievable using one tier alone.

1.2. Network Design Optimization Philosophy

The “optimization” of any system inherently invokes the balance of competing parameters. Very broadly, the optimal design may be one that achieves a balance between the cost and performance of a system where gains in performance are associated with an increased cost. Alternatively, if financial and labor limitations are a barrier to implementing a high-cost network, a low-cost network can be implemented at the expense of performance.

For a methane monitoring network, performance might be defined as the ability to detect a leak, or further, to determine the leak’s location, or quantify a leak’s emission rate. The end user might also consider incorporating the spatial and temporal coverage of a monitoring network. While an obvious definition for cost is the capital cost of materials (e.g., monitoring equipment and data purchases), it is also important to consider the labor required to operate and maintain a monitoring network.

The practicality of deploying monitoring assets will be impacted by the resources, funding, and authorizations that have been granted to an administering organization. These constraints should be considered when establishing definitions of cost and performance and can be used to refine the scope of the network design optimization. Because many practical details are unknown to the authors of this report, it is impossible to recommend a detailed design for a monitoring network. Rather, we present an optimization framework and discuss some of the broad insights that it provides.

1.3. Optimization Framework Overview

In this section we establish a performance metric and a workflow that was implemented to evaluate that metric for different monitoring network configurations. Under this framework, we first ask our workflow to simulate a spatially resolved methane concentration field using an array of environmental inputs including assumed emission rates for facilities. Methane measurement values from a given network design are then inferred from the simulated concentration field. These values are then used to infer a concentration field which is then utilized to infer emission rates at known source locations. We then compare the inferred emission rates to the assumed (i.e., ground truth) emission rates that were used simulate the methane concentration field and leverage the accuracy of that inference as our performance metric.

This workflow is visually depicted in Figure 3 and is described as follows:

1. **Source terms:** The user aggregates source term and environmental information relevant to the domain where a monitoring network will be deployed. This information includes the source locations, emission rates, and meteorology.
2. **Atmospheric transport modeling:** The source term and environment information is incorporated into a model to simulate methane as it is transported to from the leak location to the surrounding environment.
3. **Simulated concentration field:** the atmospheric transport model provides a spatially resolved methane concentration field.
4. **Network design:** The user provides the workflow with a prospective design for the methane monitoring network. This includes information about the tiers of measurements that are used, the locations of those measurements, and the performance of the monitors being used to make those measurements (e.g., accuracy, sensitivity, etc.)
5. **Measurement inference:** Using the simulated methane concentration field and network design information to simulate measurements.
6. **Data fusion:** Inferred measurements are assimilated.
7. **Inferred concentration field:** The data fusion process provides an inferred concentration field.
8. **Source attribution:** Using the inferred concentration field, source attribution is performed.
9. **Inferred emission rates:** The source attribution algorithm provides inferred emission rates that can be compared to source term emission rates (used in step 1).

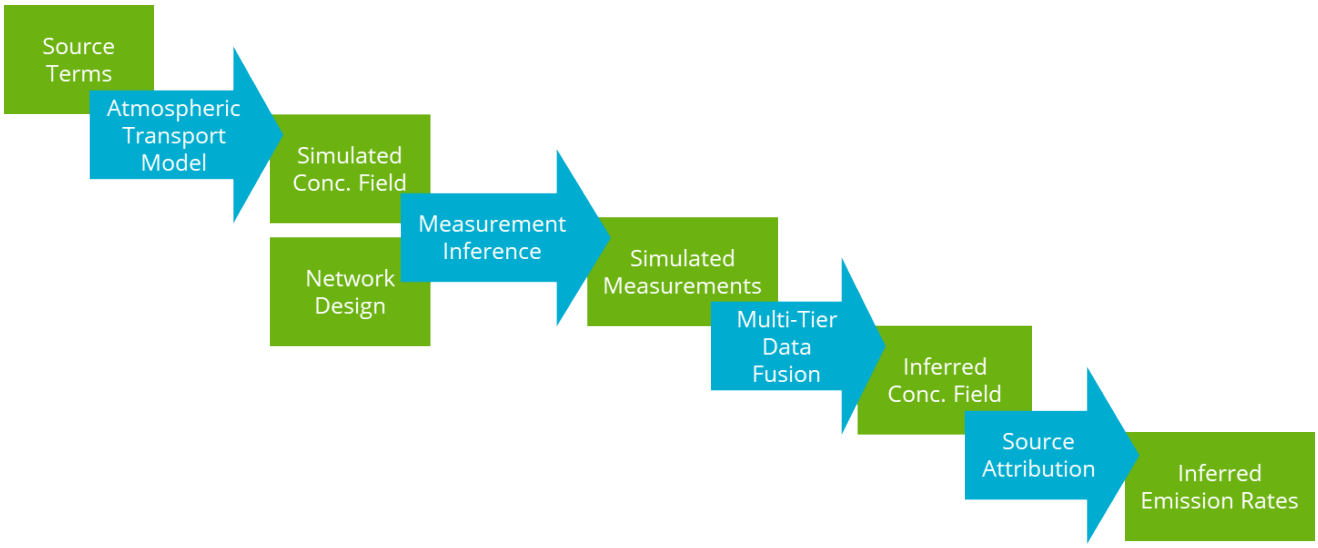

Figure 3: A schematic of the workflow used to evaluate the performance of a prospective methane monitoring network.

1.4. Report Structure

Section 2 of this report describes the source term information and the model that was used to generate simulated methane concentration fields. Section 3 describes network design parameters that a user might consider. This includes different satellite, aerial and ground-based sensing platforms and their associate performance statistics. This section also provides insights into how measurement inferences are developed and reports on the characteristics of simulated measurements provided by each of these modalities. Finally, Section 4 provides a description of how data fusion of simulated measurements is used to infer a concentration field and, subsequently, perform source attribution to infer emissions rates. This section also provides a discussion of the network performance evaluations the relies on the comparison between input emission rates and inferred emission rates. Section 4 first describes probabilistic optimal sensor placement under a Tier 2-3 network against budget and monitoring constraints before constructing a fully integrated (Tier 1-3) monitoring system and both a Bayesian inverse model and inverse Gaussian plume model to learn underlying emission rates. Section 5 discusses the importance of biogenic flux modeling in accurately determining background methane concentrations, and for non-O&G methane sources. Finally, Section 6 concludes with a discussion of our results and scope for future work in methane monitoring.

2. SIMULATING A METHANE CONCENTRATION FIELD

As previously discussed, the first steps of our network evaluation workflow require the simulation of a spatially resolve methane concentration field. An atmospheric transport model is used to produce this simulation. That simulation must be informed with source term parameters and environmental information. This section details the input information and model that we leveraged to perform this simulation.

2.1. Source Locations and Descriptions

Well pad locations in the Permian Basins were referenced from the New Mexico Oil Conservation Division (OCD) database. While OCD provides a wealth of data regarding the current and historical operational state of production facilities in New Mexico, critical information needed to quantify emissions estimates, such as detailed component counts, are not reported. While we have considered ways that diagnostics reported by OCD may enhance our simulations in the future, only location data is utilized for this analysis.

2.2. A Stochastic Model for Methane Emission Rates

Methane emissions from the oil and gas industry are highly variable in scale and duration. For instance, maintenance events such as compressor blowdowns have a total duration of 15 minutes or less but may exhaust over 100 kg of methane in that short time frame. In contrast, a small leak from a pneumatic controller may be continuous, but typically have emission rates that are less than 0.1 kg/hr. Emission events are also challenging to predict. While some venting, flaring, and maintenance events are permissible and expected under normal operating conditions, upset events occur irregularly due to faulty equipment components, downstream pipeline capacity limitations, or other operational challenges. At any given time, an amalgamation of different emission events may be occurring in a basin or subsection of a basin.

Given the level of complexity and variability of these events, an emissions model is needed to accurately represent emissions scenarios for a geographic area of interest. Rutherford et al. (2021) developed such a model that is based on a synthesis of data from several measurement campaigns. Their model provides stochastic component level emissions that we have used to develop facility and

basin level emissions for different scenarios. For this analysis, we limited our focus to oil and gas production facilities and assumed that each facility was identical and comprised of the component counts listed in Table 1.

Table 1. Component counts used for emission estimates to simulate methane concentration fields.

Component Type	Component Count
Well	1
Header	1
Heater	2
Separator	2
Meter	1
Tank - Leaks	3
Compressor	1
Dehydrator	0
Injection Pump	1
Pneumatic Controller	1

2.3. Meteorological Data

Hourly meteorological data is utilized from the Hobbs, NM station. Meteorological conditions are assumed to be spatially uniform across the entire Permian basin. Meteorological conditions are also assumed to be vertically uniform across the 100 m in altitude that are modeled in this effort. While the simulations could be enhanced by leveraging spatially varying meteorological with a finer temporal resolution (e.g., minute data rather than hourly data), this data provides enough fidelity and relevance to compare different monitoring designs in a relatively localized geographic region.

2.4. Simulating the Dispersion and Advection of Methane Emissions

Once emission events have occurred, meteorological conditions including wind speed, stability, turbulence, temperature, and relative humidity impact how quickly the resulting plume is advected and dispersed in the atmosphere. Therefore, meteorological conditions must be considered when evaluating the detectability of a plume. For example, when wind speed is low and atmospheric conditions are stable/not turbulent, effluents may not be transported far from the emission source. Thus, under these conditions, effluents will not be subject to rapid dispersion and the plume will be more concentrated. While effluents may not be transported to a detector that is relatively far from the source, nearby sensors will have a higher probability of detecting emissions from the source than under windy and turbulent conditions. Conversely, if wind speeds are high and conditions are unstable or turbulent, effluents have a higher probability of being transported to distant sensors, but nearby sensors will have a lower probability of detecting emissions than during low wind speed and low turbulence conditions.

Given the complex behavior of plumes from methane leaks, evaluating the ability of a methane network to detect leaks requires a model that can emulate this complex behavior. This section of the report describes and justifies the use of a such a model, details the characteristics of plume representations from this model, and provides an agnostic overview of how plume detectability varies across different meteorological conditions, leak rates, and instrument sensitivity.

A plethora of computational tools exists that can be used to represent plumes from emission sources. To determine which tool is most appropriate, a user must consider the spatial scale, temporal variability, the thermodynamic properties of the plume, as well as how physically rigorous the representation of the plume should be and what level of fidelity can be resolved with the information available.

For this application, it is not necessary or even possible to use a physically rigorous model (e.g., computation fluid dynamics) since we are making broad generalizations about the source terms associated with methane plumes and the environment within which that plume is dispersed. For efforts described later in this report, it was also necessary to employ a model that is computationally inexpensive to facilitate an analysis that requires many iterations of the model across various conditions. We will consider more complex models for future development and operational use of the

framework presented in this report, such as a gaussian puff model or a DNS. These models are attractive for a plethora of reasons such as their ability to use spatially resolved meteorological and environmental conditions to evaluate the evolution of effluents over many timesteps. Nonetheless, a gaussian plume model is adequate for simulating localized dispersion of emissions like acute methane leaks and are even implemented for regulatory applications (e.g., AERMOD).

A simple version of a gaussian plume model is described by the following equation:

$$C(x,y,z) = \frac{Q}{2\pi\,\sigma_y(x,y)\,\sigma_z(x,z)\,u} e^{-\left(\frac{h^2}{2\sigma_z^2}+\frac{y^2}{2\sigma_y^2}\right)}$$

where C is the concentration of an effluent at a downwind distance, y, from the source, and a crosswind distance, x, from the plume centerline. In this form of the gaussian plume equation, Q is the mass emission rate of the effluent at a point source with an effective stack height, h. The speed of the wind is incorporated with u. The rate with which the plume is dispersed in the horizontal and vertical directions is described by the dispersion coefficients, σ_y and σ_z, respectively. These coefficients are calculated for a given downwind (x), crosswind (y), and vertical (z) distance from the source and are also dependent on the Pasquill-Gifford stability class.[66] Even this simple gaussian plume model incorporates substantial complexity and is sensitive to an array of source term and environmental parameters.

3. SENSOR TIERS AND DESCRIPTIONS

3.1. Tier 1: Satellite Sensors

As satellite sensing technologies continue to advance, their role in environmental monitoring is expanding. Spaced-based sensors (which we define as Tier 1 sensors in this analysis) are now being used to improve low-resolution emission estimates for a variety of gaseous and particulate pollutants. Platforms such as the Sentinel-5P and GOSAT-2 can be used to reconcile global and regional methane emission inventories. More recently, the GHGSat platform has delivered data with enough fidelity to detect facility level emissions. A complete list of methane monitoring satellite payloads and their performance metrics, including the new Carbon Mapper, are provided in Table 2.

Though satellites have the advantage of providing methane monitoring global coverage, most payloads cannot take measurements with a high enough spatial resolution or sensitivity to provide significant value for methane leak detection efforts. Further, while more low-altitude systems capable of large methane leak detection are slated to be deployed in the coming years, these systems are severely limited by revisit times that are longer than 15 days. Given that many methane emissions are highly variable and have durations less than an hour, even geosynchronous orbiting platforms with one day revisit times do not provide adequate temporal coverage.

Nonetheless, the considerable (and increasing) volume of openly available data provided by these platforms should not be disregarded and as discussed later in this analysis, can be synergized with other sensing modalities to enhance methane detection capabilities.

Table 2: Satellite platforms and performance metrics.

Satellite or Mission	Operator	Pixel Dimensions (km x km)	Revisit Time (days)	Precision (σ) (%)	Swath Width (km)	Lower Det. Threshold (kg/hr)	Coverage	Reference(s)
MERLIN	DLR/CNES	0.12	28	1 - 2			Global	20, 21
Copernicus CO2M	ESA, EC	2 x 2	5	0.60	250		Global	22
Feng Yun 3G (CMA)	CMA-NMSC	13.7 x 13.7			1200		7 spots across swath	23, 24
G3E	ESA	2 x 3	0.083	0.50			Central Europe	25
GaoFen-5	CHEOS	12 x 13			2600			26, 27
GEO-CAPE	NASA	4 x 4	0.042	1.00				28, 29, 30
GEOCarb	NASA	3 x 6	0.083 - 0.33	0.60	2800	4000	North & South America	29, 31, 32,33, 34
GEO-FTS	NASA	3 x 3	0.083	0.20				35
GOSAT	JAXA	10 x 10	3	0.70		7100	Global	36, 37
GOSAT-2	JAXA	10 x 10	3	0.40		4000		38
MethaneSat	EDF - Env. Def. Fund	0.4 x 0.1	3-4	0.1-0.2	260	200	200 × 200 km targets	39, 40

Satellite or Mission	Operator	Pixel Dimensions (km x km)	Revisit Time (days)	Precision (σ) (%)	Swath Width (km)	Lower Det. Threshold (kg/hr)	Coverage	Reference(s)
MetOp-SG	EUMETSAT	7 x 7	1	0.60	2670			41
MicroCarb	CNES	4.5 × 9	7	0.70			13.5 × 9 km targets	42
PCW/PHEOS-WCA	CSA, Canada	10 x 10	0.083				arctic	43, 44
SCIAMACHY	ESA	30 x 60	6	1.50				45
Sentinel-5P (precursor)	ESA, NSO	5.5 x 7	1	0.60		4200	Global	46, 47, 48
ADEOS-1	NASDA, Japan	8 x 8		4.00				49
ADEOS-2	NASDA, Japan	8 x 8		4.00				49
AIRS	NASA	45 x 45	0.5	1.50			Global	50, 51
Aura	NASA	5 x 8		1.00			Global	52, 53
Joint Polar Satellite System	NOAA	14 x 14	0.5	1.50	2200		Global	54, 55
Carbon Mapper	NASA	0.03 x 0.03			~10	~10-25	Targeted high-emission regions	

3.2. Tier 2: Aerial Sensors

Another class of monitoring systems that are being rapidly developed includes those deployed on aerial platforms (e.g., plane and drones). These systems are capable of surveying large swaths of oil and gas production basins, facilitating the surveillance of hundreds of facilities in a single flight. Aerial systems are typically outfitted with standoff detectors that take total column methane measurements between the surface and flight attitude (approximately 1000 m). Commercial and government platforms have successfully demonstrated the detection of methane plumes with leak rates lower than 50 kg/hr.

Though aerial surveys have revolutionized our ability to detect and attribute methane to persistent leak events, the labor and costs of these surveys are a barrier to achieving continuous monitoring, which is necessary to detect intermittent and short duration leak events.

A list of methane imagers that can be deployed on aerial platforms is provided in Table 3. A list of fixed-wing and rotary aerial sensor platforms is provided in Table 4 and Table 5.

Table 3. Methane imagers deployed on aerial platforms and performance metrics.

Satellite or Mission	Sensor Type	Wavelength Range (nm)	Spectral Resolution (nm)	Pixel Size (km)	Swath Width	Emission Rate LOD (kg/hr)
AVIRIS-NG	SRS	1600-1700, 2200-2510	5	0.003		16
Kairos	SRS					46-52
Carnegie Airborne Observatory-2	SRS and LIDAR	365-1052, 380–2510, 1064	5		34°	
Ball Aerospace Methane Monitor	LIDAR	1650				~1
Carleton University, Ottawa	DIAL	1600		0.002	0.128 km	0.6

Table 4: Fixed-wing UAV methane monitoring platforms.

Model	Wing Length	Load Weight	Speed	Endurance Time	Flight Distance	Flight Height	Reference
RQ-4	35.4 m	3000 lbs.	650 km/hr	32 hr		20,000 m	15
Believer Fly v2.2	1.96 m	1.5 lbs.		2 hr	20 km		16
Mightly Fly		100 lbs.			1000 km		17

Table 5: Rotary UAV methane monitoring platforms.

Model	Load Weight	Speed	Endurance Time	Flight Distance	Flight Height	Reference
Inspire 2	0.8 kg	58 mph	0.5 hr	7 km	2500–3000 m	18
S-100	50 kg	220 km/h	6 hr	200 km	5500 m	19

3.3. Tier 3: Ground Sensors

A ground-based sensor is defined as a sensor that is installed at or near ground level. This can include fixed or stationary detectors, sited at facility fence lines and nearby towers, or mobile sensors that are mounted on vehicles. Ground-based sensors also operate in standoff (similar to those implemented on aerial platforms) or in situ configurations.

Singh et al. (2021) conducted an evaluation of the field performance of methane sensing systems. In general, the ground-based sensors used in this study reported sensitivities and lower limits of detection between 3 and 300 ppb, which corresponds to lower leak rate detection limits between 0.2 to 20 g/hr at close proximities (10 m to 100 m). It should be noted that these systems are state of the art, are relatively expensive, and have varying degrees of operational autonomy.

Motivated by the growing need for large scale comprehensive leak detection, there has been a recent emergence of low-cost methane monitoring technologies. However, these sensors are limited by their lack of sensitivity, poor accuracy, sensor-to-sensor variability, and dynamic range. Honeycutt et al. (2019), provided statistics describing the poor sensitivity and signal noise of low-cost sensors and reported lower limits of detection and signal variability (standard deviation) ranges of 16.3 ppm to 170 ppm and 5.4 ppm to 37.1 ppm (RMSE range of 15% to 24%), respectively. While the performance of these sensors inhibits their use for environmental monitoring that requires sub-ppm sensitivity, they have some utility for near-field detection of moderate to large leaks.

Table 6. Ground-based methane sensors and performance metrics.

Sensor	Limit of detection	Sensitivity /Precision (1σ) (ppb)
General Tools (GT)	0.05 kg/m^3	0.5
ATO Portable	0.003 kg/m^3	0.3
Picarro	0.001 kg/m^3	0.22

3.3.1. Ground Sensor Zones of Detection

Leveraging the previously described gaussian plume model, we define a Zone of Detection (ZOD) as the volume of plume with a concentration of effluents that is sufficiently high enough to be detected by a sensor with a certain sensitivity. ZOD size is sensitive to three parameters: the emission rate of a leak, the meteorological conditions under which those emissions are dispersed, and detector sensitivity. Figure 4 provides a visual depiction of a ZOD and defines dimensional parameters that can we use to conceptualize the utility of sensors for leak detection: ZOD length, width, and height. ZOD length and width are the downwind and maximum crosswind extents of the ZOD, respectively.

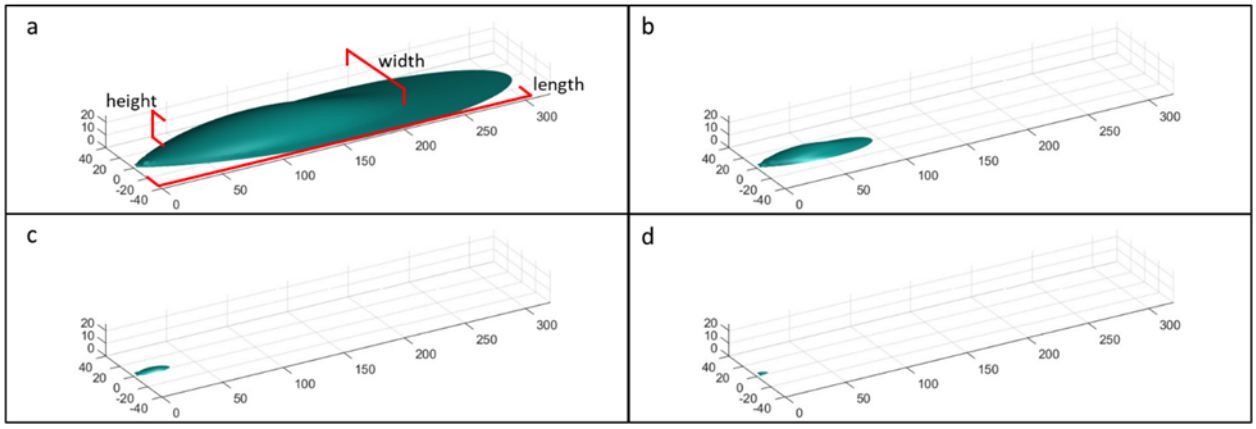

Figure 4: ZOD for sensors with sensitivities that are (a) 10%, (b) 100%, (c) 1000%, and (d) 10000% above background methane concentrations. Panel (a) visually depicts ZOD length, width, and height with the highest sensitivity above background to observe the plume. ZODs are simulated assuming a leak rate of 100 kg/hr and a wind speed of 10 m/s. The x-, y-, and z-axes report the downwind, crosswind, and vertical distance from the source in meters.

For this analysis, we evaluate how the width, length, and height of a ZOD varies across this parameter space which includes:

- Emissions rates: 1 to 1000 kg/hr
- Wind Speed: 1 to 7 m/s
- Incoming solar radiation: “moderate” for all cases
- Detector sensitivity: 10% to 10,000% above background [CH_4] (2.1 ppm to 191.9 ppm)

Figure 5 through Figure 7 report the ZOD length, width, and height, respectively, as a function of the wind speed normalized leak rate (Q/U) for sensor sensitivities ranging from 10% to 10,000% above background concentration. Aside from the demonstrating the trivial trend of increasing ZOD with increasing sensor sensitivity, this analysis can be used to develop a conceptual design for ground sensor placement. Assuming that 100% and 1000% above background sensitivities ZODs are analogs for the detection of state-of-the-art highly sensitive sensors (e.g., Picarro) and low-cost sensors, respectively, the ZOD length analysis suggests that moderate leaks with a Q/u value of 10 (kg/hr)/(m/s) (or a leak rate of ~10 to 70 kg/hr) can be detected by a state-of-the art sensor at a downwind distance of 100 m or less and that super emitters (Q/u ≥ 100 (kg/hr)/(m/s)) can be detected at a downwind distance of 300 m or more. In contrast, low-cost sensors need to be within a downwind distance of 20 m and 100 m respectively to detect the same moderate and super emitter leaks. While it's likely not fiscally or operationally feasible to locate state of the art sensors 100 m downwind of every oil and gas production facility, it may be possible to deploy or site multiple low-cost sensors in close proximity to each oil and gas facility (or a prioritized subset of facilities).

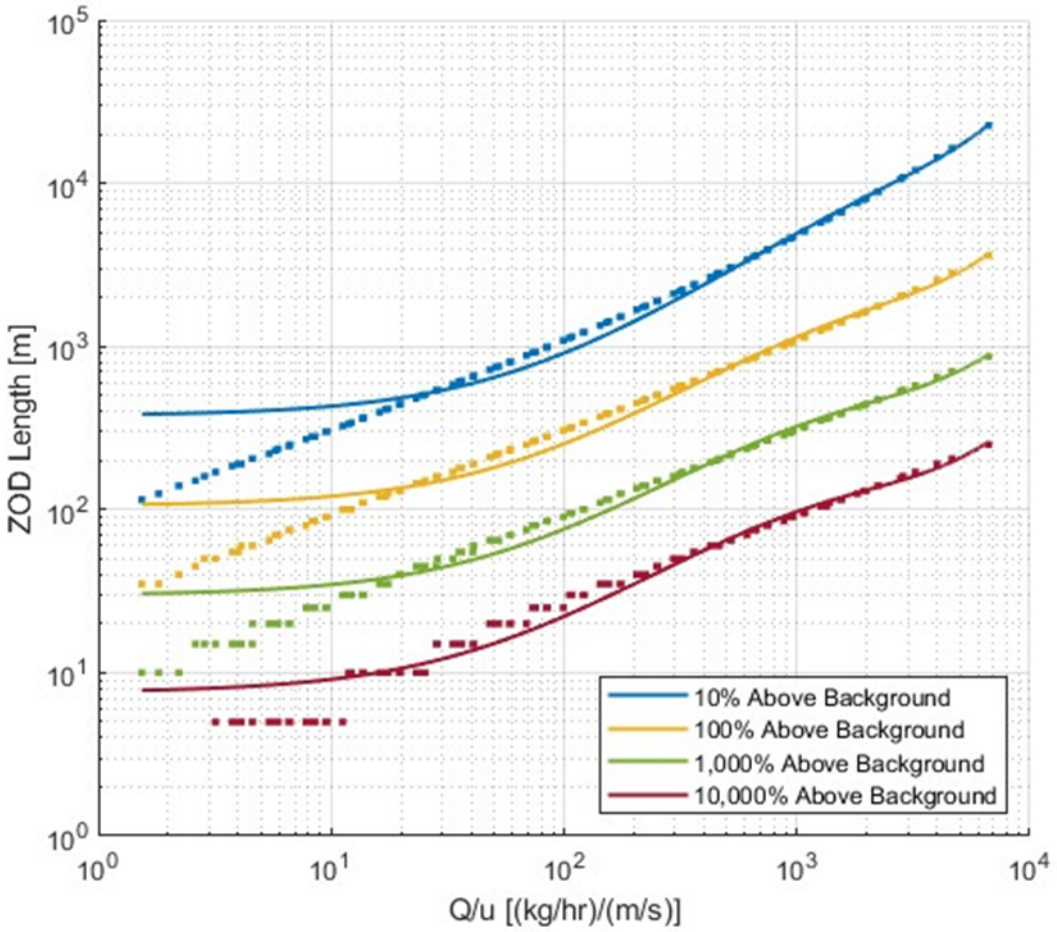

Figure 5: ZOD lengths as a function of Q/u for different instrument sensitivity proxies expressed as percent greater than the background CH4 concentration. Data points represent individual modeled scenarios. Solid lines represent an exponential fit of the form Y = a*exp(b*x)+c*exp(d*x).

Whereas the ZOD length analysis provides insights on the downwind siting requirements for detection, noting the variability of wind direction, the width analysis can be used to consider the crosswind spacing required to optimize detection frequency. Retaining our existing definitions for detector sensitivity proxies, moderate leaks, and super emitters, this analysis indicates that a low-cost sensor would need to be placed at crosswind distance increments of ~25 m or less to achieve comprehensive detection of super emitters. If we assume that the sensors are placed on a circle with a radius that is approximately the distance from the center of the facility to the fence line (~50 m), comprehensive super emitter detection would require over 10 fence line sensors per facility assuming plume motion

with minimal buoyancy. Though these sensors are low-cost, the cost to outfit a facility with more than 10 sensors is unreasonably high, especially when the costs associated with sensor maintenance and calibration are taken into consideration. However, the placement and density of sensors can be further optimized by leveraging sensors placed at other nearby facilities and by considering probabilistic wind speeds and directions from local climatological data.

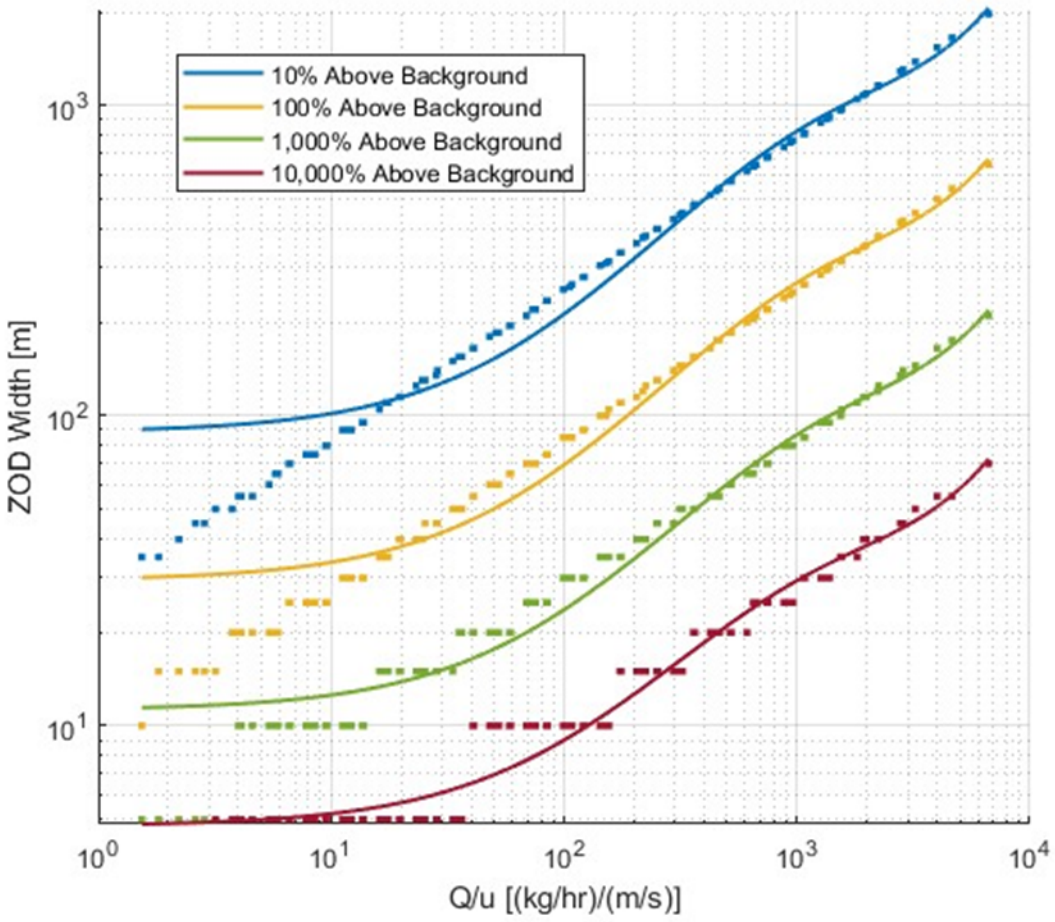

Figure 6: ZOD widths as a function of Q/u for different instrument sensitivity proxies expressed as percent greater than the background CH4 concentration. Data points represent individual modeled scenarios. Solid lines represent an exponential fit of the form Y = a*exp(b*x)+c*exp(d*x).

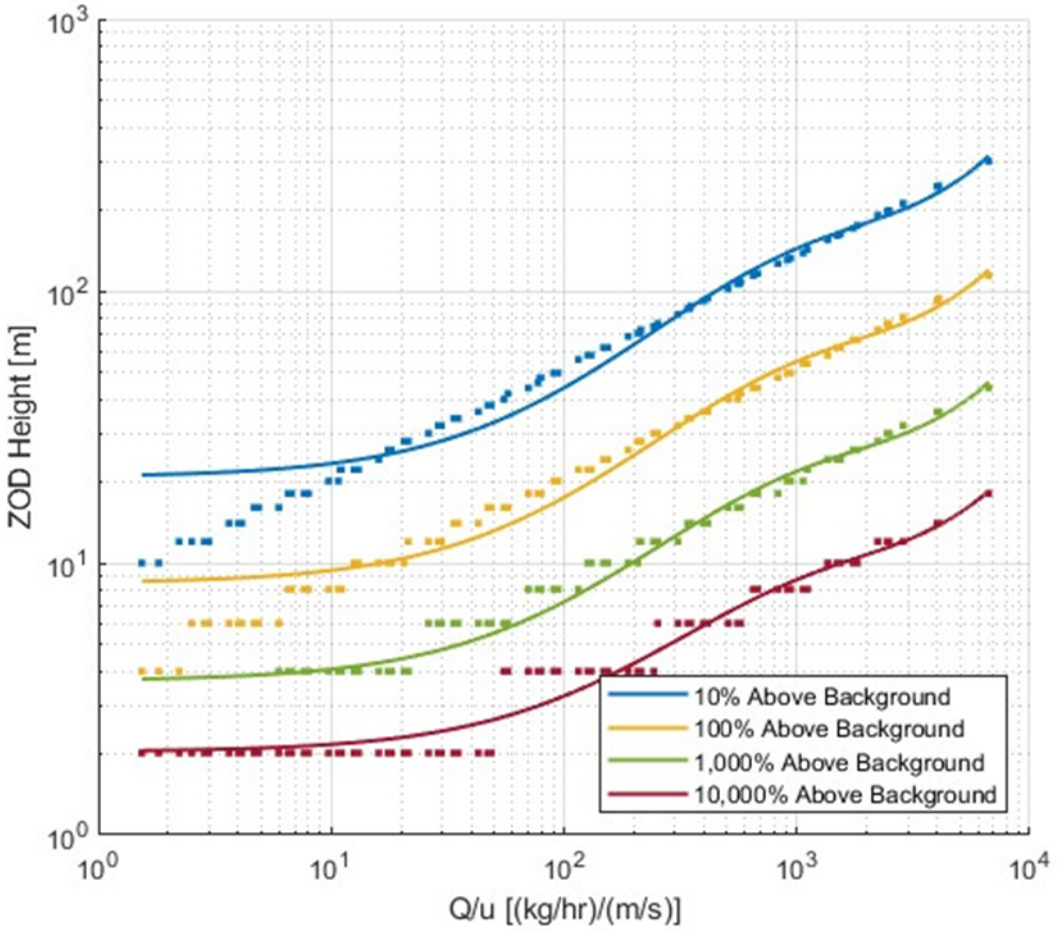

Figure 7: ZOD widths as a function of Q/u for different instrument sensitivity proxies expressed as percent greater than the background CH4 concentration. Data points represent individual modeled scenarios. Solid lines represent an exponential fit of the form Y = a*exp(b*x)+c*exp(d*x).

3.3.2. The Potential Utility of Mobile Sensors for Leak Detection

Several additional factors must be considered when evaluating a mobile sensor's ability to detect methane leaks. Since the sensor's position is not static and therefore will only be within a leak's ZOD temporarily, the data acquisition rate and response time must be considered in addition to the other performance factors previously discussed for stationary sensors. These necessary considerations challenged our ability to perform a robust analysis on the ability of mobile sensors to detect methane leaks, but a scoping analysis was performed to evaluate what portion of leaks are in close enough

proximity to roads to be detected by mobile sensors. The leak locations and road segments were defined using datasets reporting the locations of well pads and road segments for the entire Permian Basin.

For this analysis we simulated plumes using a matrix of conditions defined by the following parameter ranges:

- Leak Rate: 1, 10, and 100 kg/hr
- Wind Speed: 0.1, 1 and 10 m/s

Since this analysis was not informed by wind direction, a simplified detectability metric was adapted: a leak is considered to be detectable if it is located within a distance from a road that is less than or equal to the leak's ZOD length at a height of 1 m (the approximate height of a mobile detector). A detailed description of the methodology and GIS workflow used to conduct this analysis is reported in Appendix A. Recognizing that this analysis will overstate the detectability of sensors due to the omission several important factors, these results nonetheless provide a valuable upper bound estimate of the fraction of leaks in the Permian Basin that can be detected with mobile sensors.

Figure 8 shows the percentage of wells in the Permian Basin that are monitorable as a function of ZOD length. There are three groups of data, Group A representing those ZODBs where the ZOD length is less than 1000 meters (Red), Group B with zone lengths greater than and equal to 1000 meters but below 6000 meters (Green), and Group C (blue) with zone lengths greater than and equal to 6000 meters. The plot shows that for the case when we consider a ZODB of greater than or equal 1000 meters for all wells, the percentage of monitorable wells at that size is at least 95%. This means that the ability to monitor leaks of greater than or equal to 1000 meters with mobile Tier 3 sensors is excellent. In Group B, we see a slightly diminished ability and in Group C the ability to monitor wells degrades quickly as the ZOD length drops.

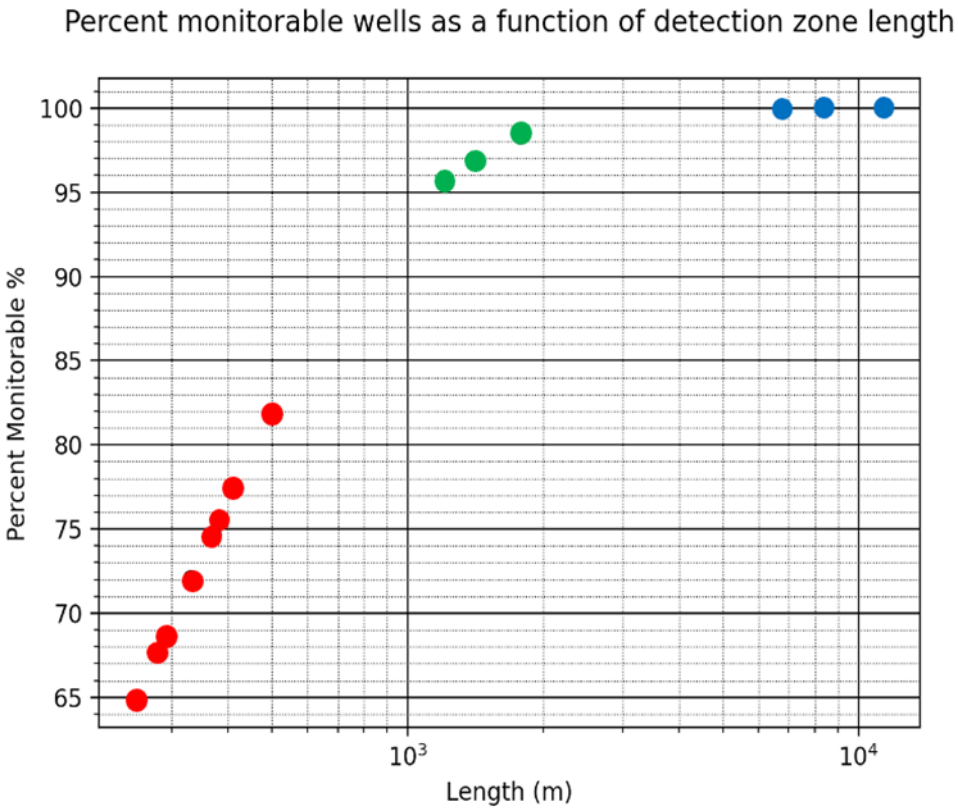

Figure 8: Percent of wells monitorable by Tier 3 sensors for various ZOD lengths. There are three groups of data, Group A representing those ZODBs where the ZOD length is less than 1000 meters (Red), Group B with zone lengths greater than and equal to 1000 meters but below 6000 meters (Green), and Group C (blue) with zone lengths greater than and equal to 6000 meters.

An extension of this analysis showing the geographic areas with insufficient road coverage to detect leaks ("dead zones") is provided in Appendix B.

4. FULLY INTEGRATED SENSOR NETWORK

In this section, we provide a robust end-to-end modeling workflow that can ingest tiered sensor measurements to determine overarching methane concentration maps and underlying emission rates from individual sources, such as those provided by the well data that we have studied over the Permian basin. In doing so, we first demonstrate robust sensor placements with both stationary and mobile ground sensors (Tier 3), that can additionally be placed on towers/posts (Tier 2), and mobile sensors able to be carried by low-flying drones (Tier 1) over areas of interest. To aid in the design of the integrated sensor network, we leveraged prior work done at Sandia through the creation of Chama, open-source software for sensor placement optimization. The Chama framework can probabilistically account for various wind conditions in its optimization routines, allowing for more effective sensor placement. Using the learned knowledge of optimal sensor placement, we subsequently propose a multi-tier modeling framework that hierarchically combines all tiers' sensor measurements. We first show that this multi-tier representation can quantify a data-fused methane concentration map that provides a richer visualization of potential leaks across higher fidelity spatial and temporal resolutions than any one tier alone. Second, using inverse Bayesian modeling, we demonstrate the framework's robustness in accurately learning underlying leak locations and their emission rates (source attribution) with quantifiable uncertainties, thereby providing a benchmark decision-making capability for identifying potential leaks using a tiered monitoring system. Due to challenges associated with quantifying the accuracy of source attribution based upon varying sensor and meteorological conditions from the inverse Bayesian model, we subsequently use inverse Gaussian plume modeling to study the impact of source attribution by demonstrating algorithm sensitivity to instrument accuracy, sensor density and standoff distances.

4.1. Integrated Sensor Set-up for the Permian

Sandia's Chama software informs design of a sensor network and establishes a monitoring strategy which minimizes environmental impact given a limited budget. Ideally, all potential emission sources could be continuously monitored using the highest sensitivity sensors and equipment, but there is a cost/benefit tradeoff between the monitoring budget in dollars and the ability to detect methane emissions. We use Chama to determine, for a fixed budget in dollars, which Tier 3 and Tier 2 sensors should be purchased, and where they should be placed, to minimize the expected amount of time to detect a methane leak. This placement not only accounts for fixed ground-level Tier 3 sensors but can include mobile Tier 3 sensors on vehicles traversing roads within biogenic and/or industrial areas containing methane emission sources, fixed Tier 2/3 sensors placed on posts or towers to measure leaks from the vertical displacement of methane plumes, and mobile Tier 2 sensors that could be deployed by drones or low-flying planes. Chama's ability to include a varied monitoring budget provides an indispensable tool to inform decision makers the degree to which methane emissions can be expected to be reduced if the monitoring budget is increased.

To reach this determinization, Chama uses information about potential emission sources, emission scenarios, including wind conditions, and their probabilities of occurrence. Given these inputs, Chama uses a mixed integer linear programming optimization routine to determine (1) which sensors should be purchased and (2) where they should be placed. Chama flexibly handles different sensor types, including point sensors, camera sensors, and mobile sensors. For mobile sensors, Chama resolves the optimal monitoring routine rather than a fixed monitoring location.

We demonstrate how Chama may be used through a case study in the Permian basin. Using historical wind data, and real-world data about potential emissions sources (i.e., oil well or facility locations as shown in Section A.1), we develop a suite of potential emission scenarios and their probabilities. For these scenarios, we use the stationary Gaussian plume model (see Section 2.4) to simulate methane emissions from a source. These, coupled with information about methane monitoring sensors on the market and their sensitivities, described in more detail below, are used as inputs to Chama to determine an optimal methane monitoring strategy. The resulting sensor network minimizes the expected amount

of methane emitted before detection while maintaining a fixed budget. For more information about Chama, the reader is directed to Klise (2017)[56].

To demonstrate optimal sensor placement, we study two areas of the Permian which can be visualized around potential emission sources and surrounding road networks as is shown in Figure 9. Both areas were chosen by their differing relative density of emission sources per spatial area, proximity to roads enabling mobile monitoring capabilities, and their spatial separation between other emission sources. Specifically, Area 1 contains 46 emission sources over an area of 8.8km^2 (5.23 sources per km^2) and Area 2 contains 38 emission sources over an area of 126.26km^2 (0.3 sources per km^2).

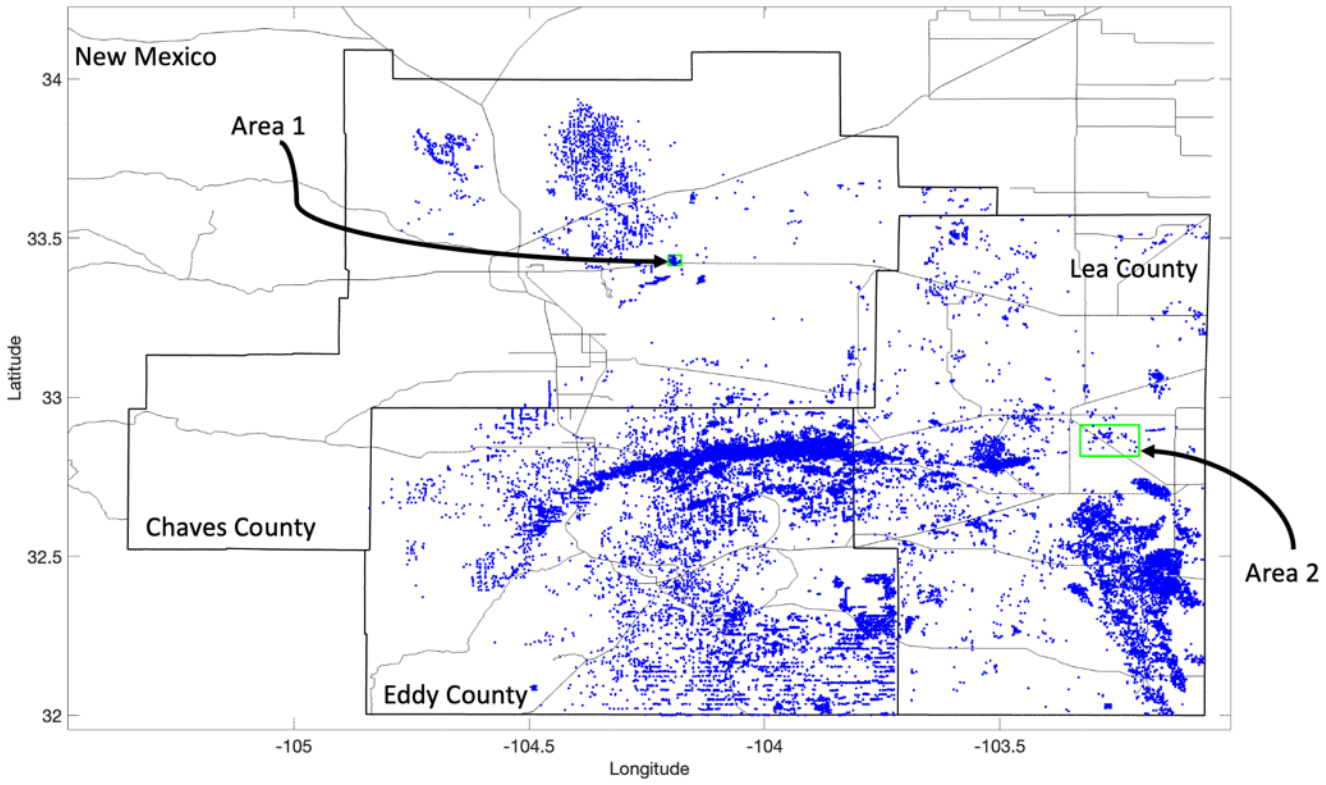

Figure 9: Two areas in the Permian Basin (green, boxed) within New Mexico counties (black, boxed) considered for Chama analyses plotted around O&G methane emission sources (blue) and intersecting roads (black, faint) for potential mobile monitoring.

For each area, we use Chama to simulate three cases: low-medium, medium-high and realistic leaks, where the latter two cases permit the occurrence of so-called *super-emitters* (emitted at >1000 kg/h). In each case, each facility's emission rate is sampled either uniformly between predefined minimum and

maximum leak rates, or from the meteorological data itself using a bootstrapped approach, as is shown in Table 7.

Table 7: Leak cases for Chama analyses with descriptions of their emission rate profiles.

Case	Minimum (kg/h)	Median (kg/h)	Maximum (kg/h)	Sampling method
Low-medium leaks	0	5.4	10.8	Uniform
Medium-high leaks	10.8	1075	2160	Uniform
Realistic leaks	0	1.08	2088	Data bootstrap

For each of the three cases, meteorological scenarios under different wind conditions (characterized by wind speed and direction) were sampled from a discretized formulation of the meteorological wind data of the Permian, which shows dependence between the two variables as presented in Figure 10.

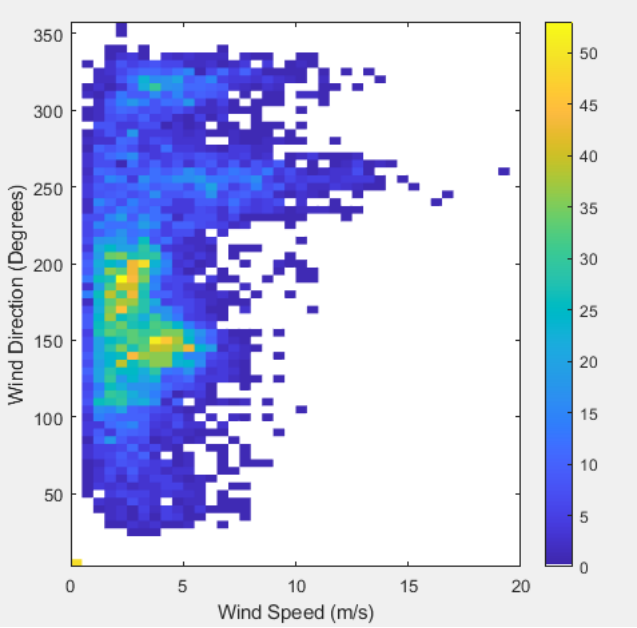

Figure 10: Distribution of wind speeds and directions of movement in the Permian at any hour, based upon historic meteorological data in the region.

In order to determine discrete scenario probabilities for Chama's formulation, the above wind data were first grouped based upon their respective Pasquill stability class [57, 58], which provides a discretized indication of the atmosphere's stability index, shown in

Table 8.

Table 8: Description of Pasquill Stability Classes indicating atmospheric stability.

Stability Class	Description
A	Extremely unstable conditions
B	Moderately unstable conditions
C	Slightly unstable conditions
D	Neutral conditions
E	Slightly stable conditions
F	Moderately stable conditions
G	Extremely Stable

In particular, by using the meteorological data from the Permian Basin, the distribution of stability classes amongst sampled conditions follows the probabilities shown in Figure 11.

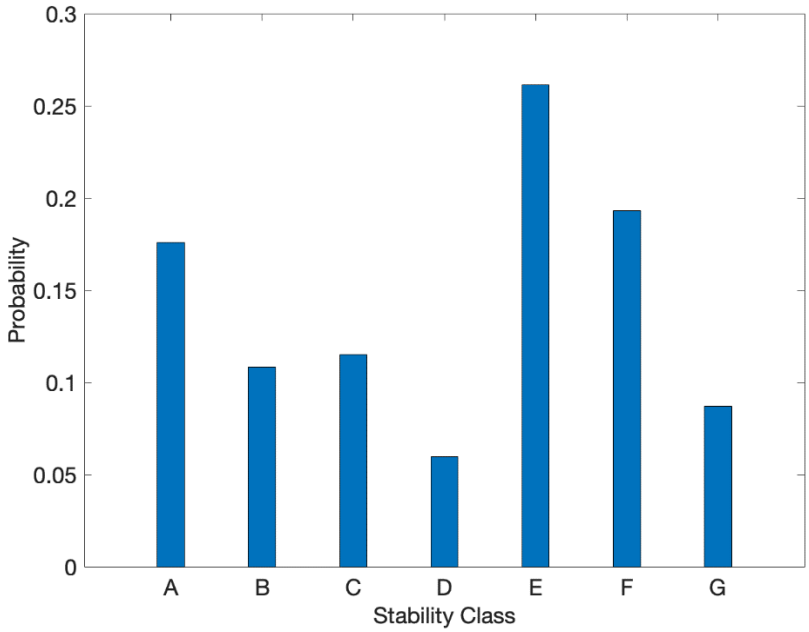

Figure 11: Time invariant probabilities of atmospheric conditions belonging to a particular Pasquill-Gifford stability class, as observed from historic data.

The stability class probabilities were used to define seven main scenarios, indicating an atmospheric condition that follows each stability class. Within each of the seven scenarios, 3 wind speeds and directions were subsequently sub-sampled from the data with sub-probabilities 0.25 (lower tail/quartile), 0.5 (median) and 0.25 (upper tail/quartile), providing the bulk of wind variability within each stability class. Under each of the seven classes, the 3 wind conditions' probabilities were determined by multiplying the sub-probability with the class probability.

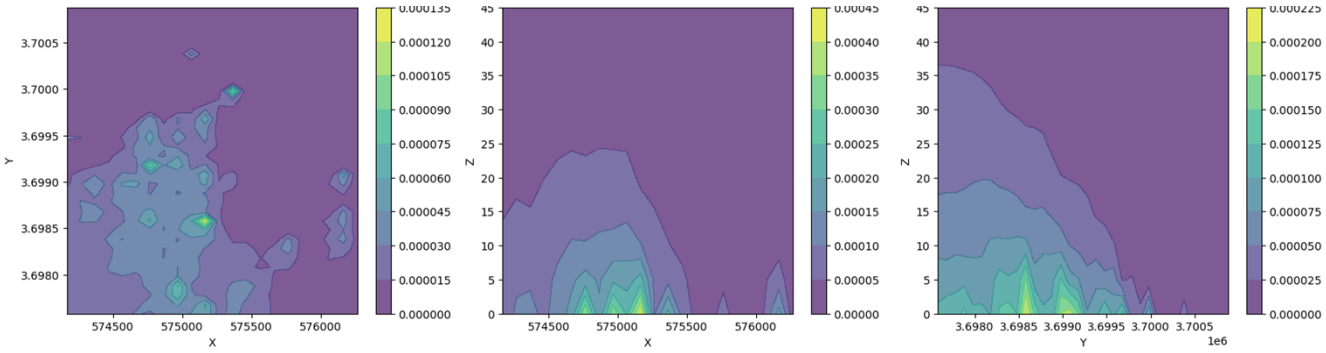

Figure 12: Realistic emission examples simulated in Area 1 under atmospheric conditions corresponding to stability class A.

In this manner, 21 different scenarios with different probabilities, characterized by wind speed, wind direction, and stability class, were determined. For each scenario, 20 independent realizations of

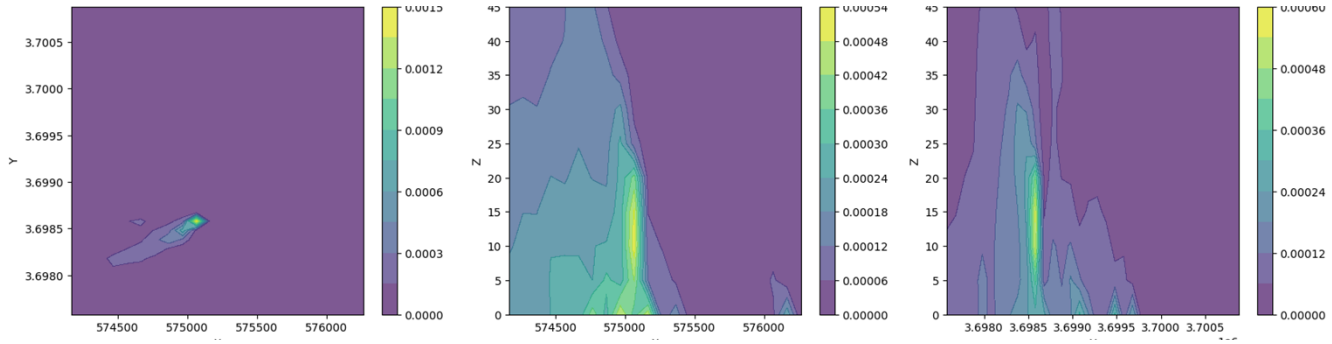

Figure 13: Realistic emission examples simulated in Area 1 under atmospheric conditions corresponding to stability class B.

methane emissions were simulated, of equal probability per leak case. In each realization, multiple leaks are accounted for via a summed Gaussian plume over the area, computed via each emission site's individual methane plume computed from its respectively simulated leak rate (as determined by the leak case shown in Table 7). In addition to accounting for the large variability in wind fields, we note the importance of accounting for multiple leaks in determining optimal sensor placements, as in reality methane leaks from O&G facilities are composed of multiple low-level leaks as opposed to an individual plume. Plume examples under realistic emission sources (sampled from historic data), and 3D cross sections under wind conditions corresponding to stability classes A-F are shown in Figures 12 to Figure 17, with color bars representing concentrations. These figures highlight the spatial variability in concentration depending on wind conditions and emission sources. The impact of the stability class can be seen by the general decrease in concentration variability/volatility across the area as the class moves from A (extremely unstable) to F (stable). Here, the x direction corresponds to the longitude (transformed to UTM in meters), the y direction corresponds to the latitude (transformed to UTM in meters) and the z direction corresponds to the vertical displacement of the plume from the ground in meters.

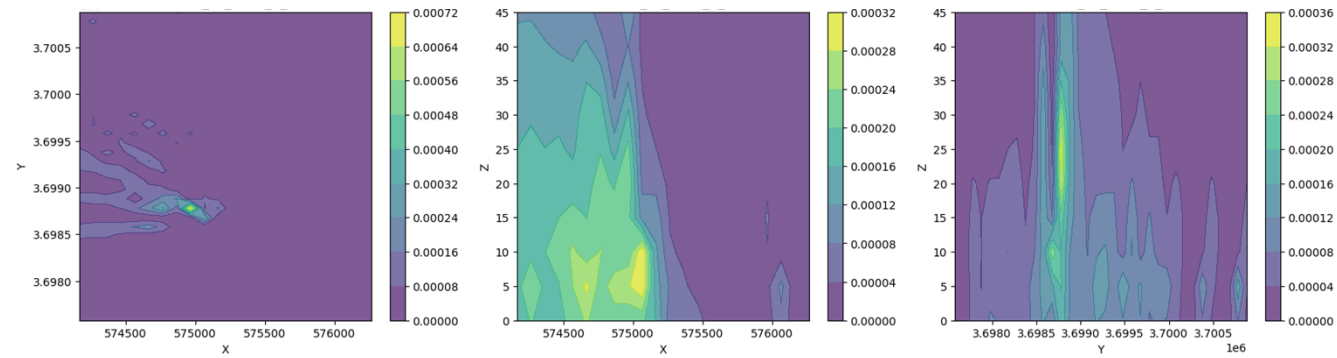

Figure 14: Realistic emission examples simulated in Area 1 under atmospheric conditions corresponding to stability class C.

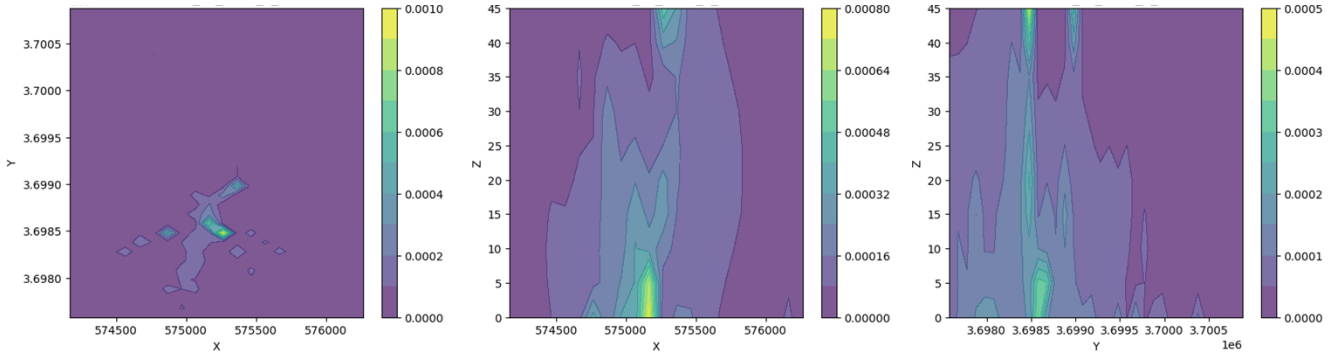

Figure 15: Realistic emission examples simulated in Area 1 under atmospheric conditions corresponding to stability class D.

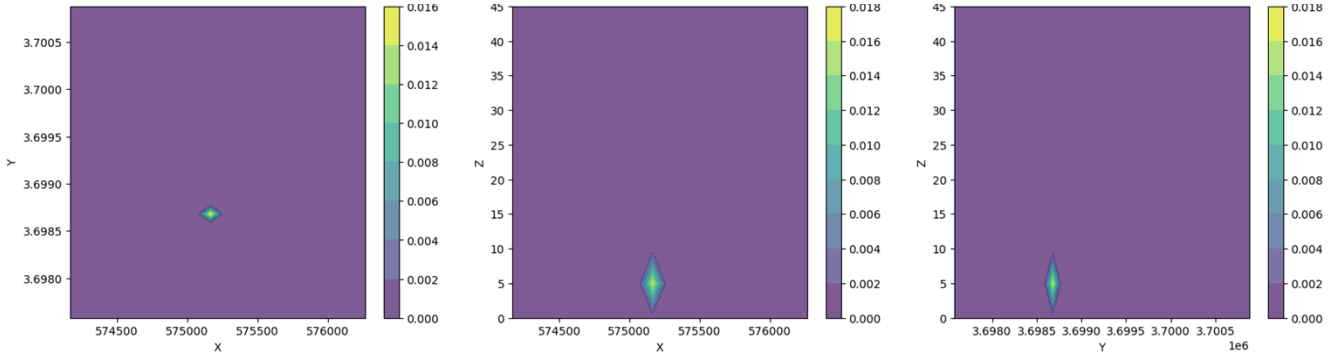

Figure 16: Realistic emission examples simulated in Area 1 under atmospheric conditions corresponding to stability class E.

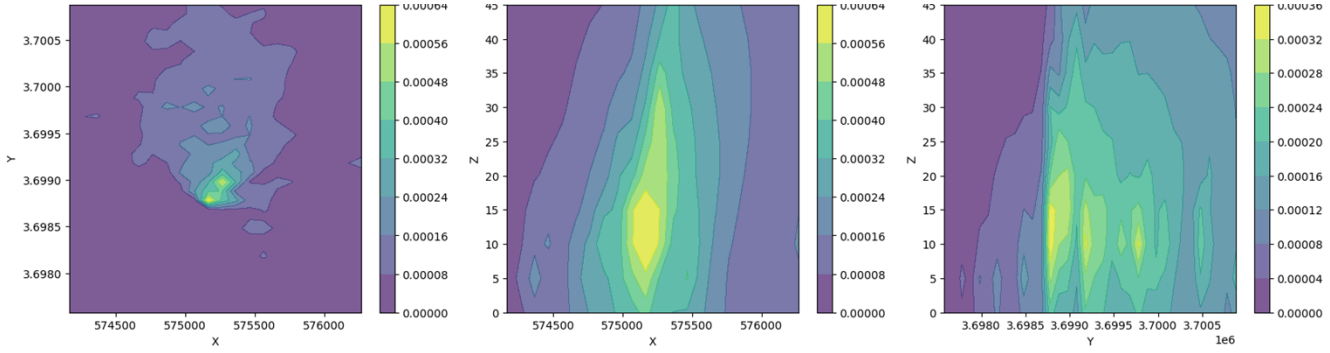

Figure 17: Realistic emission examples simulated in Area 1 under atmospheric conditions corresponding to stability class F.

In each leak case, understanding of the different scenarios via the independent realizations provided Chama with a probabilistic understanding of the most likely conditions and output in which potential methane leaks are realized. Given this understanding, Chama's optimization routines provide optimal sensor placement, constrained upon total monetary budget of sensors, which includes start-up installation costs and yearly maintenance fees. In this framework, we studied three different Tier 3 point sensors that may be situated up to 30m above ground, two different Tier 3 camera sensors amenable to mobile vehicle installation, and one Tier 2 camera sensor that may be attached to a drone, though emphasize that a larger array of Tiers 1 and 2 sensors may be analyzed in future work. The sensor specifications and budgets are listed in Table 9.

Table 9: List of sensor types considered by Chama, including potential placements, limits of detection, measurement sensitivities/uncertainties, and cost per sensor (including unit, start-up, calibration, repair, and maintenance costs).

Tier	Sensor	Sensor Type	Placement	Limit of detection	Sensitivity /precision (1σ) (ppb)	Cost ($)
3	General Tools (GT)	Point Stationary	Ground, posts (up to 30m high)	0.05 kg/m^3	0.5	$277
3	ATO Portable	Point Stationary	Ground, posts (up to 30m high)	0.003 kg/m^3	0.3	$5,050
3	Picarro	Point Stationary	Ground, posts (up to 30m high)	0.001 kg/m^3	0.22	$118,824
2/3	GMP02	Camera Mobile	Vehicle (30 mph)	10 kg/hour	Unknown	$40,000
2/3	FLIR GF77a	Camera Mobile	Vehicle (30 mph)	0.1 kg/m^2	Unknown	$60,000
2	LICOR LI-7700	Camera Mobile	Drone (15 mph)	0.9 kg/hour	Unknown	$80,000

Under both areas and with set budgets of $250,000, $1,000,000, and $2,000,000, the results of Chama's optimization routines are shown in Figure 18 and Figure 19. Interestingly, under both areas, sensor placement was optimized at around 5-10m above ground level, with no sensors placed at ground level, and a few placed at 20m above ground level. In all cases, the ground-level emission rates were sampled

using the methodology in Table 7. This determination highlights that placing sensors at ground-level is in general insufficient to capture the impact of wind on a methane leak's trajectory and emphasizes the importance of considering the vertical displacement (also monitorable via Tiers 1-2 sensors) and variable atmospheric impacts on methane plumes after emission.

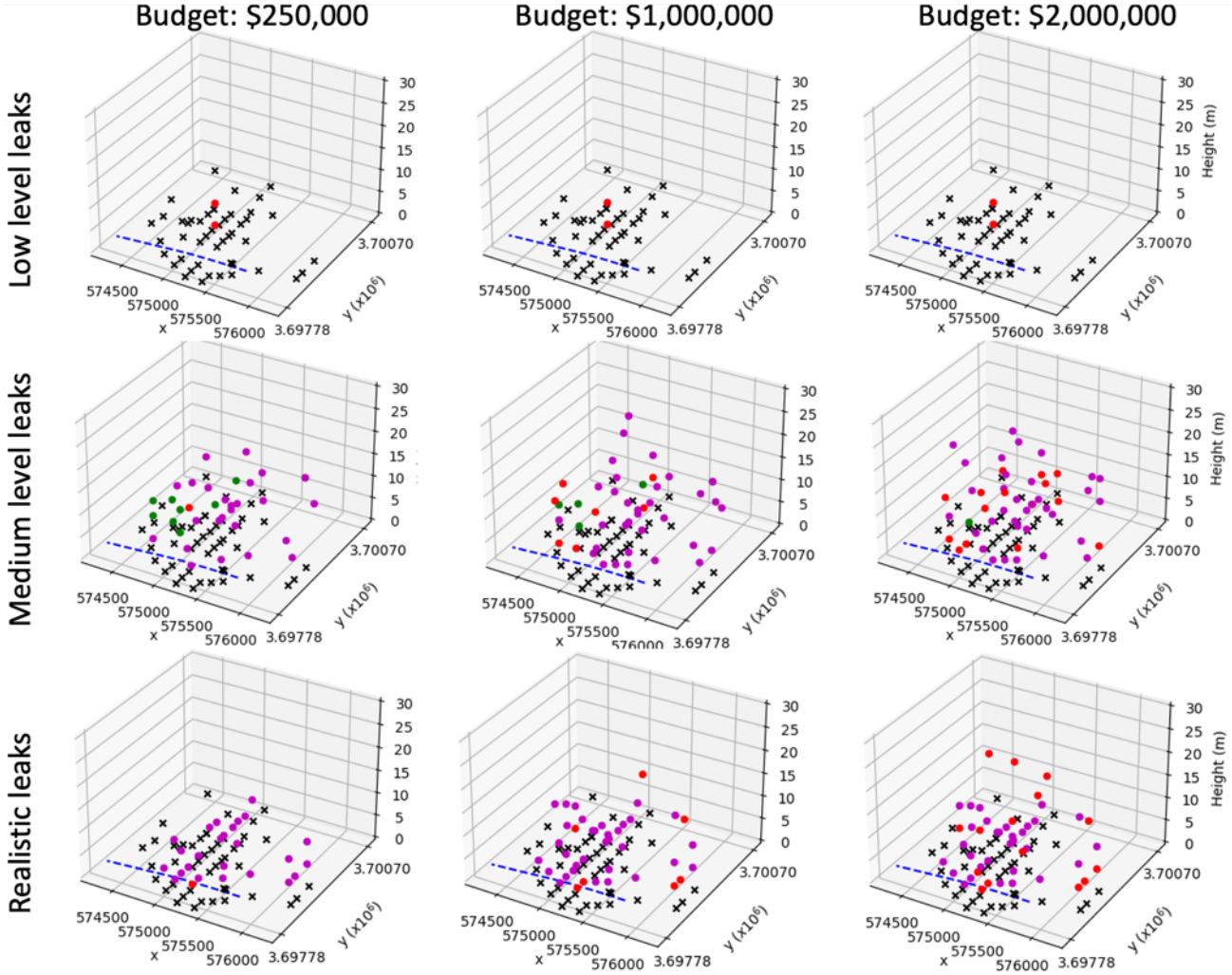

Figure 18: Optimal Sensor Placement with Chama in Area 1 of the Permian under budgets $250,000, $1,000,000, $2,000,000 and under different emulation cases (low level, medium level and realistic) as detailed in Table 9. Only stationary point sensors were chosen (between General Tools (GT) (green, circle), ATO Portable (purple, circle) and Picarro (red, circle) whose costs are listed in Table 9). Sensors are placed around potential emission sources (black, crosses) and near an intersecting road (blue, dotted).

As shown in Figure 18, optimal sensor placements are visualized in Area 1 under different leak conditions and budgets. Clearly as budget increases, more sensors are being placed in the scene. Interestingly, the cheapest point sensor (GT) is not chosen under the low-level or realistic leak scenarios under any budget due to its higher limit of detectability above background, which can be impossible to reach with lower emission rates. Under the medium-level scenario, which contains many more super-emitter scenarios, more inexpensive GT sensors are being chosen, and which decreases as the budget increases to reach an earlier detection time and increased accuracy of monitoring.

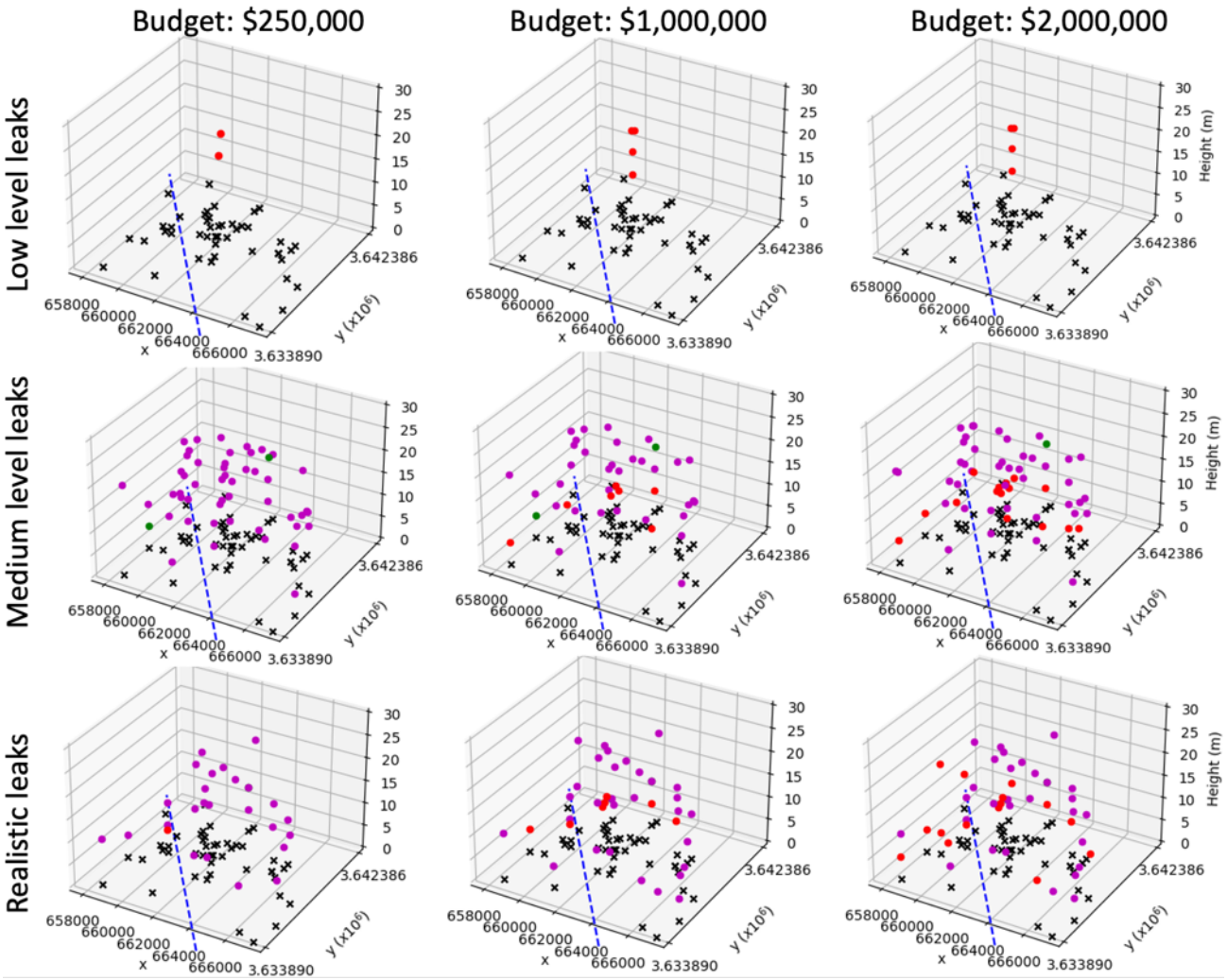

Figure 19: Optimal Sensor Placement with Chama in Area 2 of the Permian under budgets $250,000, $1,000,000, $2,000,000 and under different emulation cases (low level, medium level and realistic) as detailed in Table 9. Only stationary point sensors were chosen (between General Tools (GT) (green, circle), ATO Portable (purple, circle) and Picarro (red, circle) whose costs are listed in Table 9). Sensors

are placed around potential emission sources (black, crosses) and near an intersecting road (blue, dotted).

Figure 19 shows Chama's optimal sensor placement in Area 2 of the Permian. Generally, the same pattern of sensor choice is observed as budget and leak conditions change. Due to the lower emission rates and variable wind fields that are probabilistically accounted for in Chama, the same pattern of placing the most sensitive sensor (Picarro) at varying heights in the middle of the scene is observed under the low-level emission scenarios in both areas. Such positions are subsequently covered by chosen sensors under the medium and realistic scenarios, indicating that the detection of low-level emissions is possible under varying emission rate scenarios.

In both areas, none of the mobile sensors placed either on a vehicle or drone were picked as part of the optimal solutions. While this may be alleviated by using mobile monitoring from *point* sensors, this observation may instead be due to Chama's characterization of camera sensors. Chama's class for handling camera sensors utilizes a specific camera model[59]. Instead of determining measured signal based on limit of detection from the camera type and field of view, the detector quantifies whether a detection takes place or not by converting any signal within the camera's field of view to pixels and comparing if that exceeds the detector's threshold *in terms of pixels*. This characterization is intended to correspond to basic camera detectors placed within tens of meters of the scene and is therefore challenging to compute with camera sensor specifications for methane monitoring, such as hyperspectral or FLIR infrared cameras, especially those that are intended to cover large areas such as the Permian. As such, for the camera sensors listed in Table 9, the detection thresholds in pixels were approximated from the sensors' pixel sizes and spectral resolutions. Chama's software is therefore not optimal for determining if studied camera sensors at Tiers 1-2 are realistic for integrated methane monitoring. Instead, an important area of future work would be to modify Chama's camera sensor module to account for how state-of-the-art methane camera sensors (which could include Tier 1 satellite-level resolutions, passive spectrometers and lidar based systems) leverage their unique detection ranges, optical, and spectral properties to detect methane signals above background. Nevertheless, it is observed that Chama's placement of multiple sensors that intersect the road in each area could be leveraged with the mobile monitoring analysis conducted in Section A.1 to identify

possible routes with equipped sensors at least as sensitive as those picked by Chama for efficient mobile monitoring.

In particular, Figure 20 shows Chama's sensor placement output for Area 1 under a $2M budget around generated ZODs around each emission source emitting at 1 kg/hr at 25m altitude with a wind speed of 0.01 m/s. Here it is seen that the placed sensors are within the majority of ZODs, and those not covering a ZOD highlight emission sources close to roads that could be leveraged for accurate mobile monitoring.

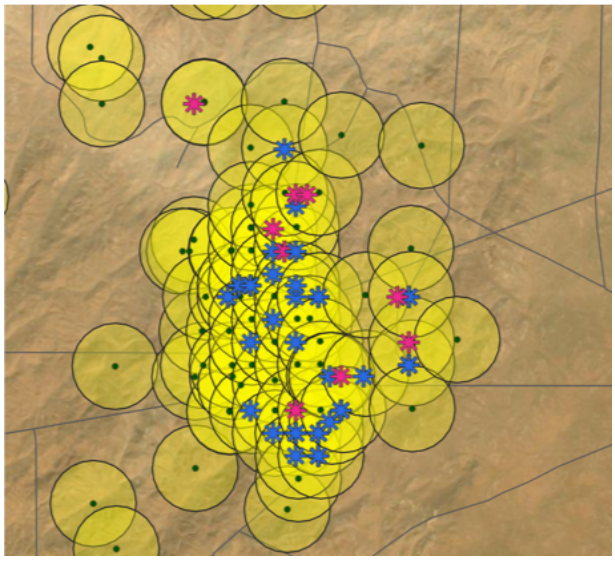

Figure 20: Chama's sensor placement of Tier 3 sensors (ATO in blue and Picarro in pink) at a $2M budget, overlaid with ZODs (yellow) computed at a wind speed of 0.01m/s at altitude 25m around each emission source (green) emitting at 1kg/h, and connecting roads in Area 1.

Importantly, Chama's framework provides a means to pursue cost-benefit analyses between sensor choice, placement, and monetary budget, which is crucial for integrated monitoring characterization and policy development. Under each leak scenario and area of the Permian considered, we can use Chama to estimate the average time to leak detection (hours) against the *covered* fraction of leak scenarios (which includes the variability in wind conditions and emission rates) detected with the sensors placed in the scene. This is to say, given the set of potential sensors and their positions, not all scenarios will be detectable, and the fraction of covered scenarios only includes scenarios that are detectable from the setup. This has a one-to-one correspondence with the monetary budget; therefore,

we consider how 1) average leak time to detection (provided by determining if a sensor with particular specification and its placement detects the leak signal over given time stamps), and 2) fraction of scenarios covered, changes as the budget increases. Figure 21 highlights this under both Areas 1 and 2, where it is seen that by just using the stationary point sensors previously considered by Chama, it takes on average at least 680 hours for a sensor to first detect the presence of a leak under the low-level leak scenario, and around 525 hours under the realistic scenario. While this calculation is done under pristine, stationary conditions in both areas, in which low emission rates were considered, these results highlight the need to consider sensor cost vs efficacy across a range of different scenarios. However, this result is to be expected with low emission rates, as a combination of several low-level leaks may be needed for the sensors to detect the advent of a breach beyond which the background concentration field is perturbed. This expected time decreases as the budget increases, where more sensors are added and the probability of at least one sensor detecting a leak increases. For medium-level leaks containing potential super-emitters, the expected time to detection decreases, and is much quicker at detection due to the higher methane concentration above background. In terms of the fraction of covered scenarios detected, Figure 21 shows a sharp increase towards 1 in all studied cases, with a smaller budget required for low-level and realistic leaks due to the limited threshold at which the given choice of sensors can be aggregated for detection. On the other hand, it is seen that more than $1M is needed in both areas with medium-level leaks to cover a higher proportion of scenarios with higher emission rates above each sensor's limit of detection. While Area 1 has a 17 times higher source per km^2 density than Area 2, Area 2's spatial area is 15 times that of Area 1. Given this, it is generally seen that a *small* but notable $250,000 increase in the budget from Area 1 to Area 2 is needed to realize the same expected times to detection and fraction of covered scenarios, which proportionally mimics the differences in density and area, and the more broadly distributed emission sources in Area 2.

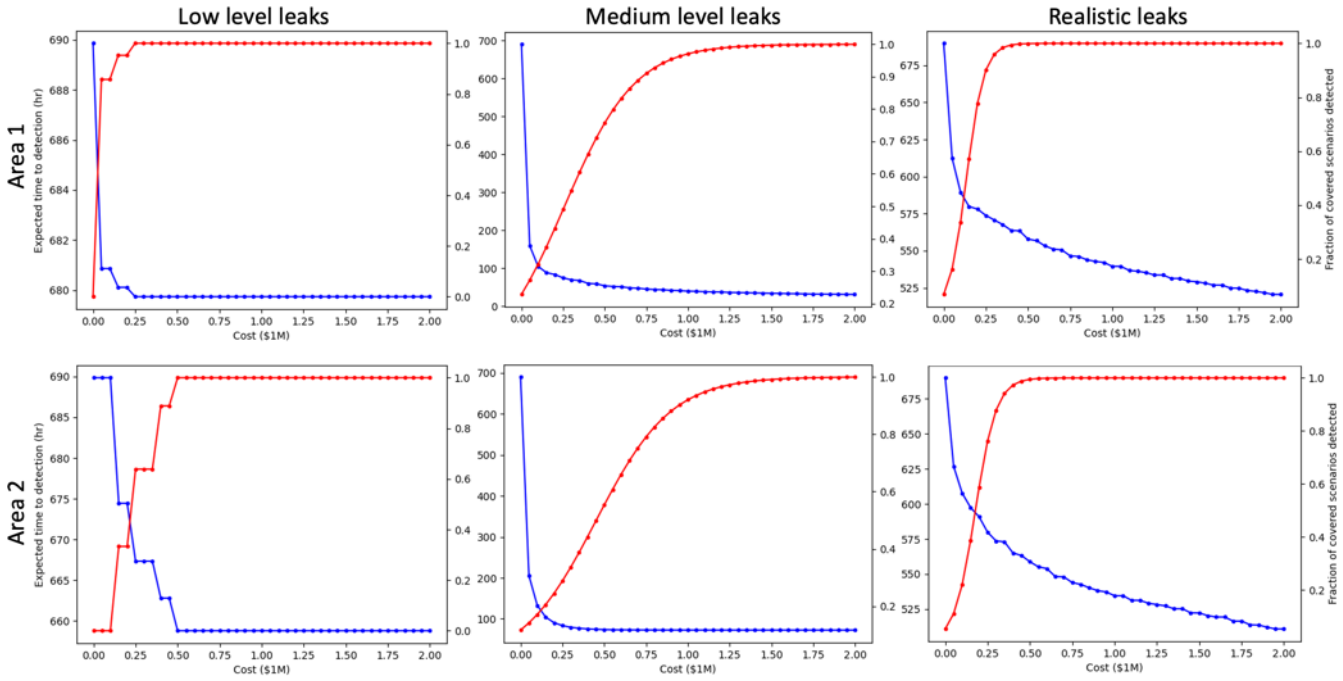

Figure 21: Cost-benefit analyses using Chama under Areas 1 and 2. Expected time to detection (blue) shown against fraction of leak scenarios covered by the optimal sensor placement (red) over budgets ranging to $2M under low, medium, and realistic leak scenarios.

Using the analyses of two areas in the Permian, we estimate that $4.2-13.5 billion in average start-up Tier 3 sensor costs over the Permian's 220,000km^2 area would maximize monitoring coverage over both sparse and densely populated emitters having realistic-high emission rates, including coverage of super-emitters. The placement of such sensors could additionally utilize Chama for optimal monitoring of leaks with relatively low (<10.8 kg/h) emission rates, as shown in the above analysis, caveated by the increased amount of time needed for detection.

With the advent of high-performance computing and Artificial Intelligence, future work involving Chama would consider many more types of stationary point and mobile camera sensors, with a larger focus on incorporating camera detectors for methane monitoring at each tier, and scalability to, for example, the spatial area of the entire Permian basin. In doing so, a larger-scale cost-benefit analysis could be conducted to find the appropriate budget possible for optimal or sub-optimal monitoring from Tier 3 and 2 sensors within the larger scope of a fully integrated methane characterization platform.

4.2. Integrating measurements across tiers

While Chama provides a basis for Tier 3 sensor placement in the Permian, an integrated monitoring system requires addition of Tiers 1 and 2 sensors for full characterization.

In order to visualize the monitoring and detection capabilities of an integrated system, we can use ideas from Machine Learning, specifically Gaussian Process modeling to fuse together the concentration data gained from each tier individually. A Gaussian Process *field* utilizes point or gridded measurements such as those provided from point or camera sensors to determine a probabilistic representation of a spatially varying object, in this case methane concentration, over a pre-defined spatial field. To visualize the power of integrating measurements between tiers, we can fit an inverse-variance weighted Gaussian Process to determine a data-fused methane concentration map. This map efficiently combines measurements from each tier based upon the relative precision of the measurement, as determined by the sensor sensitivities, and is amenable to large spatial modeling. For instance, Tier 3 point sensors have a much higher precision than Tier 1, hence the measurements obtained from Tier 3 have a higher weight in the data-fused fitting procedure. On the other hand, Tier 1-2 sensors can capture a larger, less sparse spatial field, thereby providing nonzero weight or probability to spatial areas where the absence of Tier 3 sensors render the inability to determine ground-level concentrations. An example of simulated Tier 1-3 measurements is shown in Figure 22 from simulated methane leaks in the Permian.

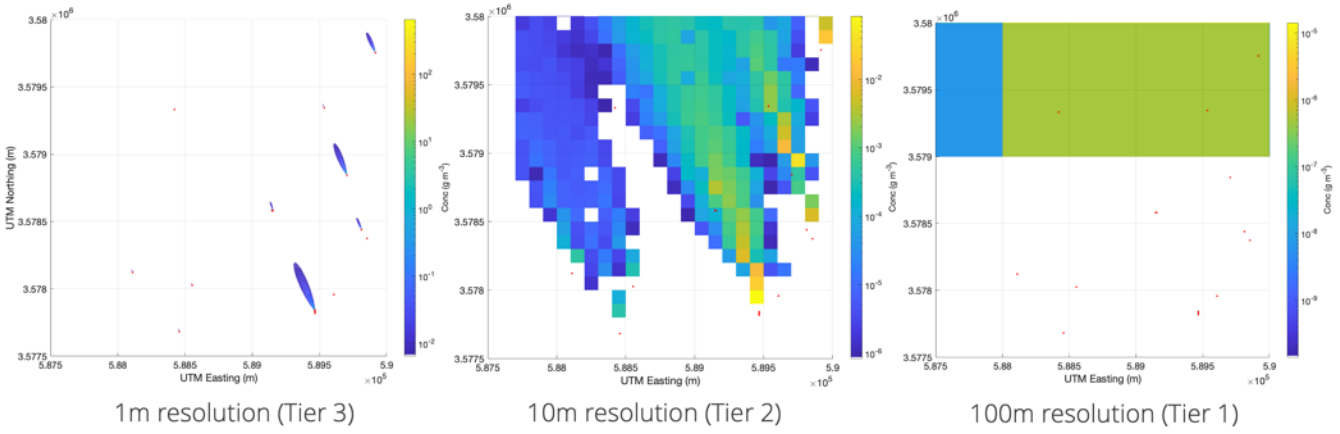

Figure 22: Example measurements of simulated methane leaks in the Permian from Tier 1-3 sensors at 100m, 10m and 1m resolution. Randomly placed ground-level (Tier 3) point sensors are shown in red.

The inverse-variance weighted Gaussian Process smoothly combining concentrations across these tiered measurements is shown in Figure 23 and highlights "hot spots" of larger methane leaks as is matched by Tier 3 measurements. Depending on the placement of ground-level sensors, an integrated methane characterization platform would therefore provide a holistic representation of methane concentration and given information from multiple tiers, could improve current leak detection times.

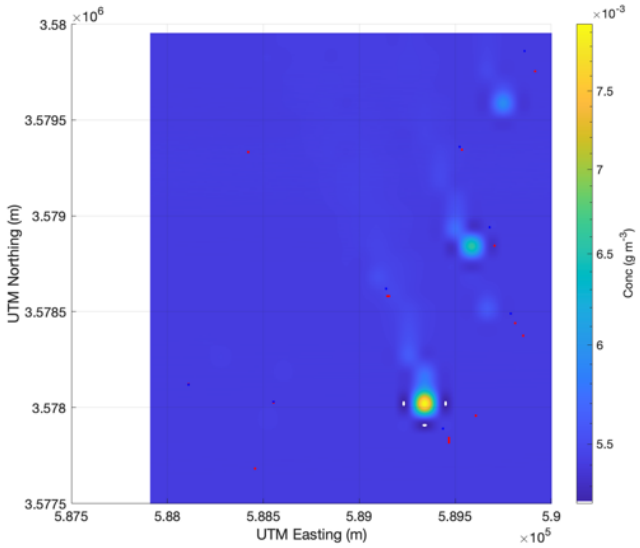

Figure 23: Inverse-variance weighted Gaussian Process smoothed concentration field determined by all measurements in a fully integrated system. Randomly placed ground-level (Tier 3) point sensors are shown in red.

4.3. Source Attribution with an Inverse Bayesian Model Approach

In order to understand the monitoring potentials of an integrated system, we utilize methane concentration measurements from Tiers 1-3 to *statistically learn* the emission rates from potential O&G emission sources in the Permian. To do so, we consider a statistical model that learns underlying emission rates given tiered observations, known wind fields and a known background methane concentration, that both separately (Figure 22) and together (Figure 23), determine a spatially varying methane concentration field. By placing Gaussian priors on the logarithm of the unknown emission rates, we utilize a similar Bayesian modeling framework to that of Weidmann et al (2022)[60], which involves continuous simulation of methane concentration fields until convergence of a set of learned emission rates that establishes concentrations that best match the tiered data. This set is intended to represent emission rates that are drawn from the (posterior) probability distribution of unknown

emission rates given (noisy) observed data. The observed data are modeled with a Gaussian distribution with mean true concentration (at a given point in space) and standard deviation (uncertainty) given by the sensitivity of the measurement obtained from that tiered sensor (see Table 9 for known instrument sensitivities). By utilizing a priori information in this framework, each iteration of the algorithm proposes emission rates that are either *accepted* or *rejected* as those from the true (posterior) probability distribution. By doing so, this framework automatically permits uncertainty quantification of the emission rates, since the collected sample is representative of the true (posterior) distribution of emission rates, from which the estimated (most likely) emission rate (distribution mode) and sample quantiles (e.g., 2.5% and 97.5%) showing the variability in the estimates, can be extracted.

Under the realistic leak scenario, we use Chama's optimal sensor placement output (with the exact sensor types and sensitivities listed in Table 9) at $1M cost, under Area 2 of the Permian (see bottom panel, center figure of Figure 21 to place Tier 3 sensors in a simulated setting. With this, we add a Tier 2 camera measurement at 100m resolution with sensitivity 10 ppbv, and a Tier 1 satellite camera measurement at 1000m resolution with sensitivity 50 ppbv. With all tiered measurements, we utilize the Bayesian inverse framework to learn emission rates from the emission sources in both Areas 1 and 2.

Overall, given the integrated sensor setup, the framework is largely able to estimate the underlying emission rates from the sources in both areas. Figure 24 provides example output from the Bayesian framework over 4 random sources in Area 2, where a point estimate (shown in green) is highlighted from the posterior distribution, including a 95% credible interval (shown in black) and the true simulated emission rate (red). In many instances which largely reflect higher emission rates (super-emitting scenarios), it can do so with high accuracy and low uncertainty. In other cases, it is unable to pick up the signal exactly, yet can provide a non-zero estimate which may still be useful for continual tiered monitoring. In these scenarios, more precise sensors at each tier, equipped with a greater monetary budget, would be needed to increase the likelihood of accurately detecting such emissions. Important future work leveraging this framework would include more efficient computation over larger spatial areas, and inclusion of time-varying observations from tiered sensors.

To emphasize the importance of the tiered monitoring system on the uncertainty quantification of emission rates from potential sources, we compare the output of this setup and framework on a) solely

utilizing Tier 3 (ground-level) sensors, b) purely utilizing Tier 3 and 2 measurements, and c) utilizing all Tiers 1-3 measurements between a randomized (i.e., randomly placed) sensor network and Chama optimized sensor network. This is shown in Figure 25, which shows the estimates, true emission rates and uncertainties across the sources in Area 1 under a fully integrated system, Tier 2-3 system, and sole Tier 3 system. Here, it is seen that while a sole Tier 3 network (shown in blue) can capture high methane leaks (super-emitters) as many high emission rates are covered within the computed uncertainty bounds, the uncertainty bounds in comparison to an optimized network are much larger. On the other hand, a Tier 2-3 system captures most emission sources with good accuracy and is largely comparable to that of a fully tiered network, with only a handful of cases where a fully tiered network is favorable (shown by true emission rates belonging to the fully tiered network's uncertainty bounds). Overall, we find that the overall error in estimating the true emission rates (across each scenario) is 1.3 times higher, with uncertainties associated with the estimates being 2.4 times higher, when using the randomized network over the Chama-optimized network. Our findings suggest that not only is a tiered approach suitable in more accurately detecting leaks, but its emission quantifications and uncertainties can be augmented by optimizing Tiers 2-3 sensors' placements.

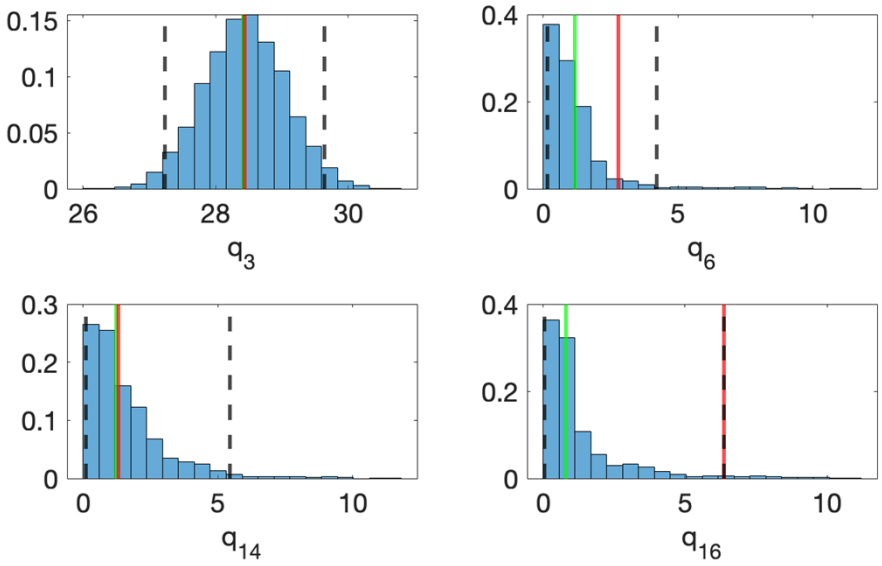

Figure 24: Sample posterior distributions of 4 randomly chosen emission sources in Area 2 of the Permian determined from the Bayesian framework showing the learned variability of true emission rates per source. From the distributions, mean estimated emission rates (green) shown with 95% credible (uncertainty) bounds (black, dotted) compared with true emission rates (red).

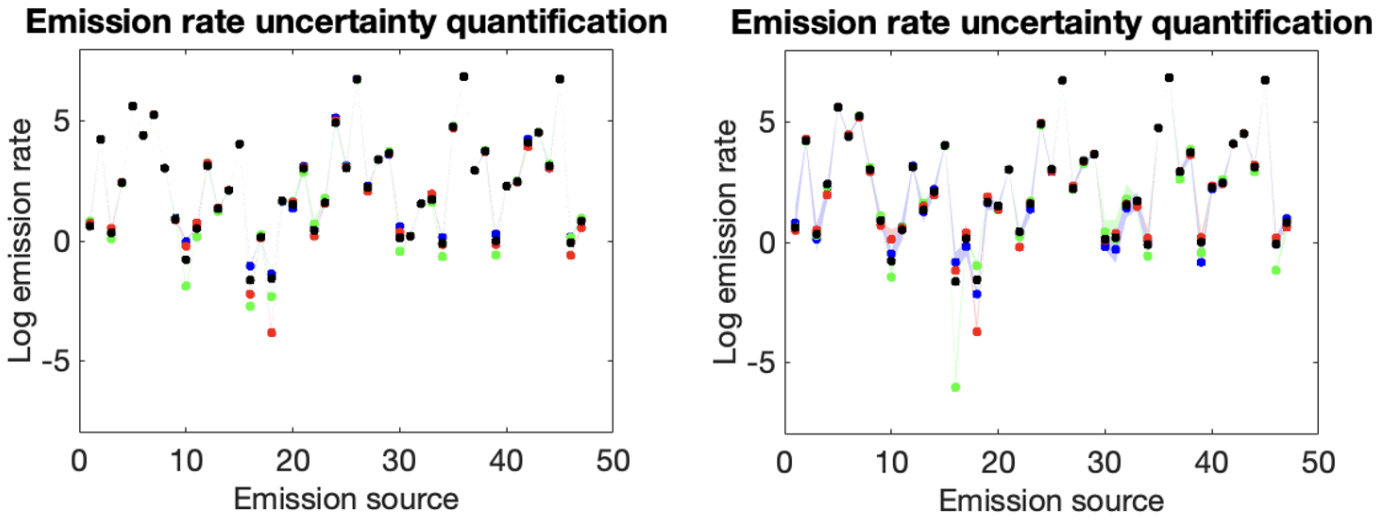

Figure 25: Comparative uncertainty quantification of emission rates from an inverse Bayesian framework under different sensor placements in Area 1: Chama-optimized placement (left) versus randomized (uniform) placement (right). Estimates are shown with circles and uncertainties are shaded, color-coded by the layered network strategy: Tier 3 (blue), Tiers 2-3 (green) and Tiers 1-3 (red). True emission rates are depicted with black circles.

4.4. Source Attribution with an Inverse Gaussian Plume Model Approach

The inverse Bayesian modeling approach presented in the previous section is advantageous in that it is able to integrate measurements from sensors across the multi-tiered network and perform emission rate uncertainty quantification for a single-scenario based on the reported accuracies of different measurement techniques. However, our implementation of this approach is limited since it does not evaluate the performance of the source attribution algorithm:

- Under a range of potential meteorological conditions;
- With spatial variability in wind speed and direction; and
- With different source emission rates.

To address the limitations of the inverse Bayesian analysis, we employ an inverse gaussian plume model algorithm that is described by the following workflow:

1. Assign receptor locations (can be a fixed location or random; sensor density can vary)

2. Randomly assign emission rates for each known source location. Emission rates are assigned based on emission rate distributions provided by Rutherford et al (2021)[61]. For this analysis, the sources located in "Area 1" were utilized (See Section 4.1).
3. Determine "ground truth" concentrations at each receptor with the previously described gaussian plume model.
4. Estimate measurement concentrations, C, at each receptor by applying random gaussian variability based on the reported accuracy for the instrument used for the measurement.
5. Determine the source contribution, G, at each sensor for each source.
6. Using a non-negative least linear squares solver, estimate the emission rate, Q, for each source. The least linear squares problem is in the form of:

$$\arg min_Q \|GQ - C\|_2^2$$

   Where Q >0.

7. Repeat the above step for 200 meteorological scenarios randomly selected from the Hobbs, NM dataset.

Several sensitivity analyses were performed to evaluate the sensitivity of a ground-based (Tier 3) sensor network's performance to:

- Instrument accuracy;
- The spatial density of randomly placed sensors; and
- The standoff distance for fixed sensors placed NE, SE, SW, and NW of each facility.

4.4.1. Sensitivity to Instrument Accuracy

Accuracy sensitivity analyses were performed on two networks: one with 50 randomly placed sensors across the spatial domain (Figure 26) and one with fixed sensors specifically placed 100 m NE, SE, SW, and NW of each facility (Figure 27).

The results in these figures show an increase in error and decrease in percent of sources detected as would be expected. However, the fixed sensor network performs significantly better than the randomly placed sensor network under virtually every scenario. Given that the fixed sensor network used 68 sensors, and the random network utilized 50 sensors, this analysis underpins the importance of optimizing sensor placement and confirms the obvious conclusion from Section 1 that sensors should be placed in areas with the most facilities. The standoff distance sensitivity analysis in Section 5.4.3 provides some important additional context.

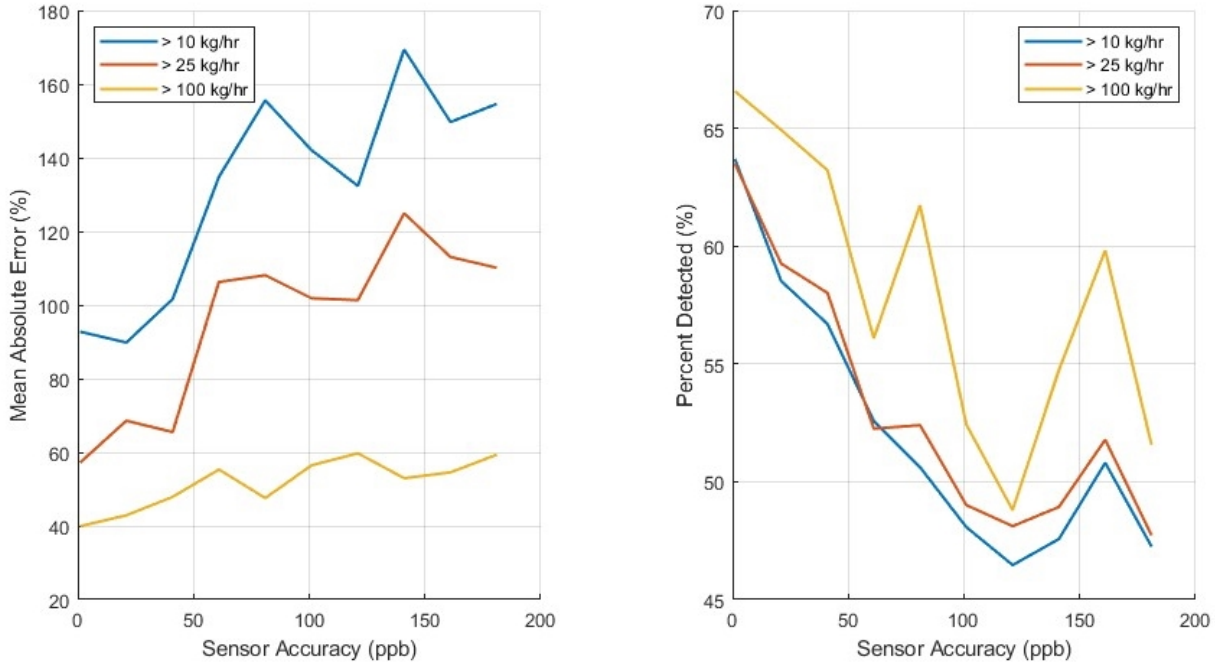

Figure 26: A sensor accuracy sensitivity analysis performed for a network of 50 randomly placed sensors. (Left)The mean absolute error of the source attribution algorithm derived emission rate vs. sensor density for different emission rate magnitudes. (Right) The percent of sources detected vs. Sensor Density for different source magnitudes.

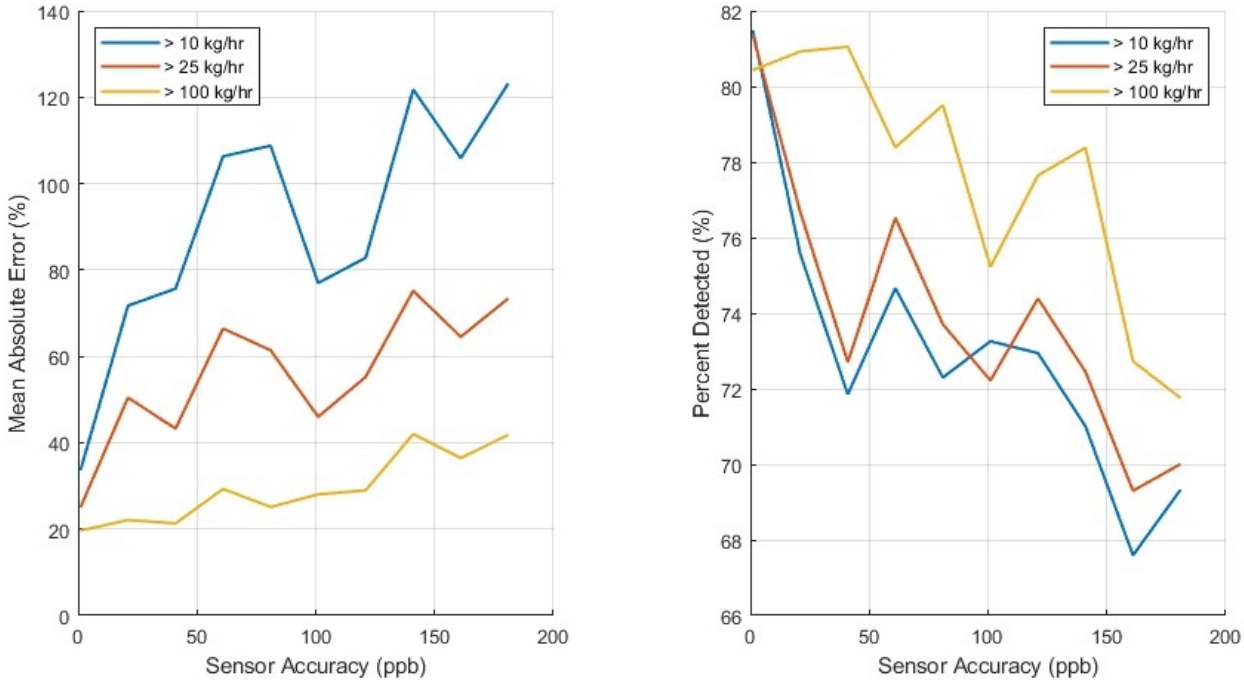

Figure 27: A sensor accuracy sensitivity analysis performed for a network sensor with fixed locations 100 m to the NE, SE, SW, and NW of each facility. (Left)The mean absolute error of the source attribution algorithm derived emission rate vs. sensor density for different emission rate magnitudes. (Right) The percent of sources detected vs. Sensor Density for different source magnitudes.

4.4.2. Sensitivity to Sensor Density

The sensitivity of performance to sensor density was evaluated on networks consisting of either all Picarro sensors (accuracy of 0.22 ppbv) or all project canary sensors (accuracy of 200 ppbv). Though an actual network could and would likely consist of a mix of these sensors, congruent to the analysis conducted in Section 4.1, this analysis comprehensively bounds the potential range of instrument performance.

Figure 28 and Figure 29 report the performance statistics of the Picarro and Project Canary sensor networks, respectively. Both figures show a decrease in mean absolute error and sharp increase in the percent of sources detected as the density of sensors increases. The network using the more accurate Picarro sensor outperforms the network using the much cheaper Project Canary sensors, however, the improvement in performance may not be significant, especially if the end goal is to detect super emitters (>100 kg/hr).

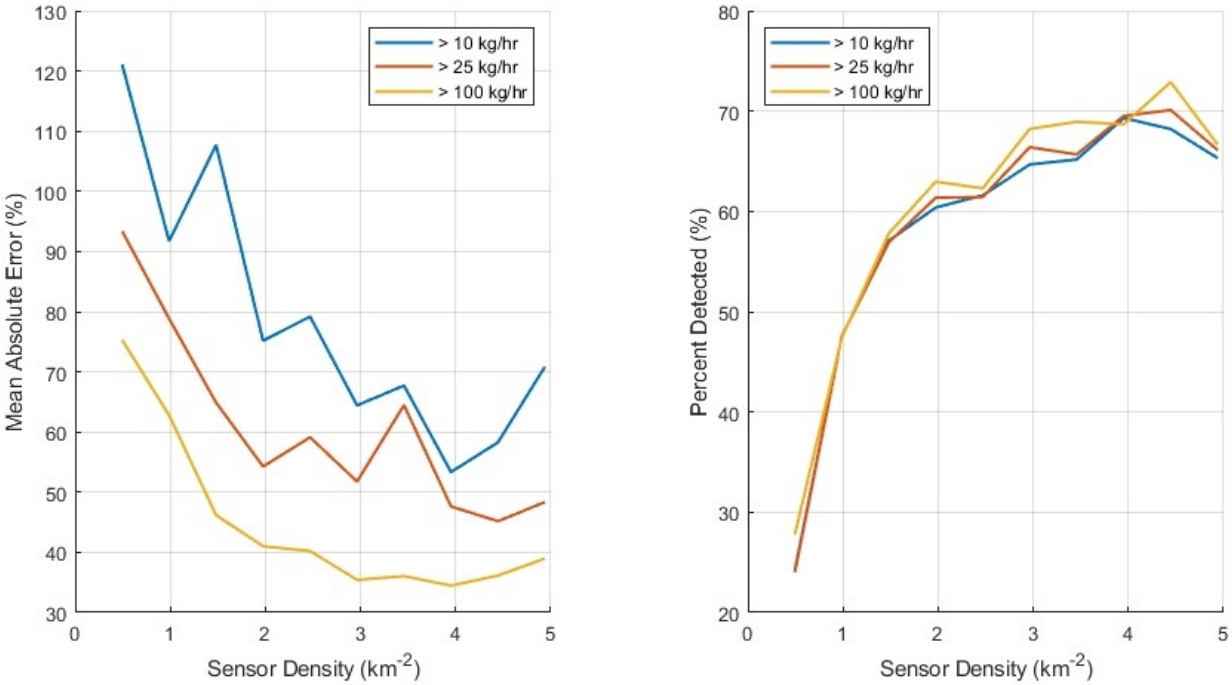

Figure 28. Sensor density sensitivity analysis performed for a network of sensors with a measurement accuracy of 0.22 ppbv. (Left) The mean absolute error of the source attribution algorithm derived emission rate vs. sensor density for different emission rate magnitudes. (Right) The percent of sources detected vs. Sensor Density for different source magnitudes.

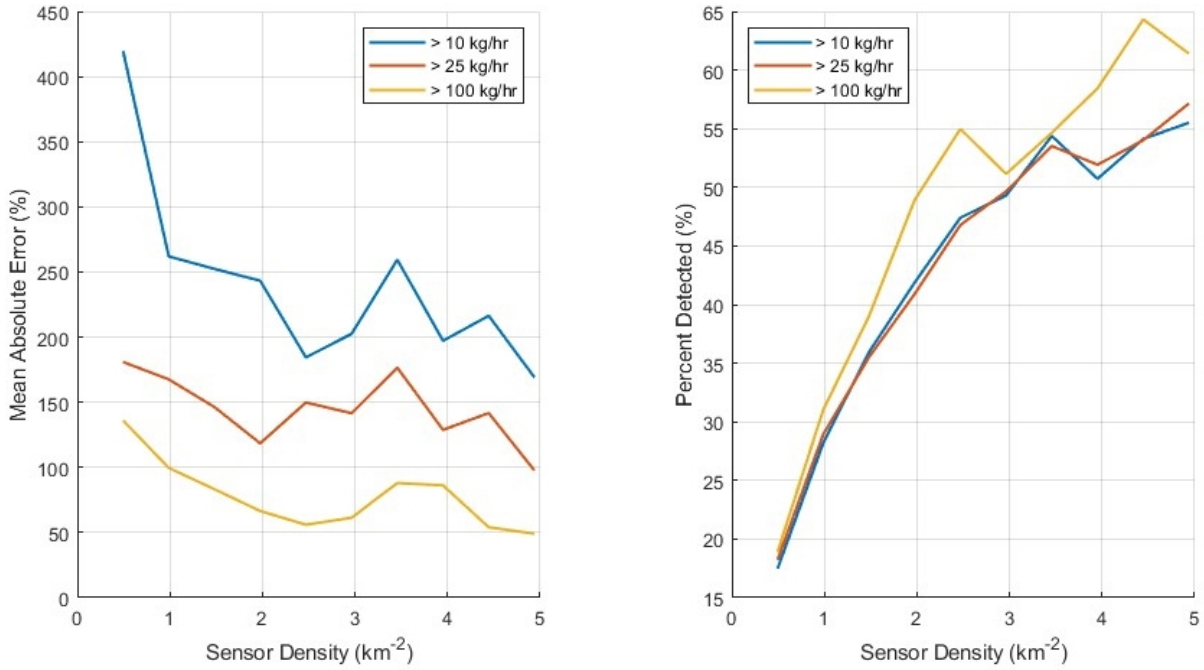

Figure 29: Sensor density sensitivity analysis performed for a network of sensors with a measurement accuracy of 200 ppbv. (Left) The mean absolute error of the source attribution algorithm derived emission rate vs. sensor density for different emission rate magnitudes. (Right) The percent of sources detected vs. Sensor Density for different source magnitudes.

4.4.3. Sensitivity to Standoff Distance

The standoff distance sensitivity analysis was conducted using the same Picaro and Project Canary sensor networks (Figure 30 and Figure 31, respectively). However, rather than conducting this analysis with randomly place sensors, a fixed number of sensors was used: four sensors placed NE, SE, SW, and NW of each facility.

The figures show that the fraction of source detected decreases as the standoff distance increases, but there is not much of a trend in the mean absolute error of the derived emission rate. The Picaro network clearly outperforms the Project Canary network in estimating the emission rate of the known sources. However, consistent with the sensor density analysis, there is not a significant increase in emission rate estimation performance between the two networks.

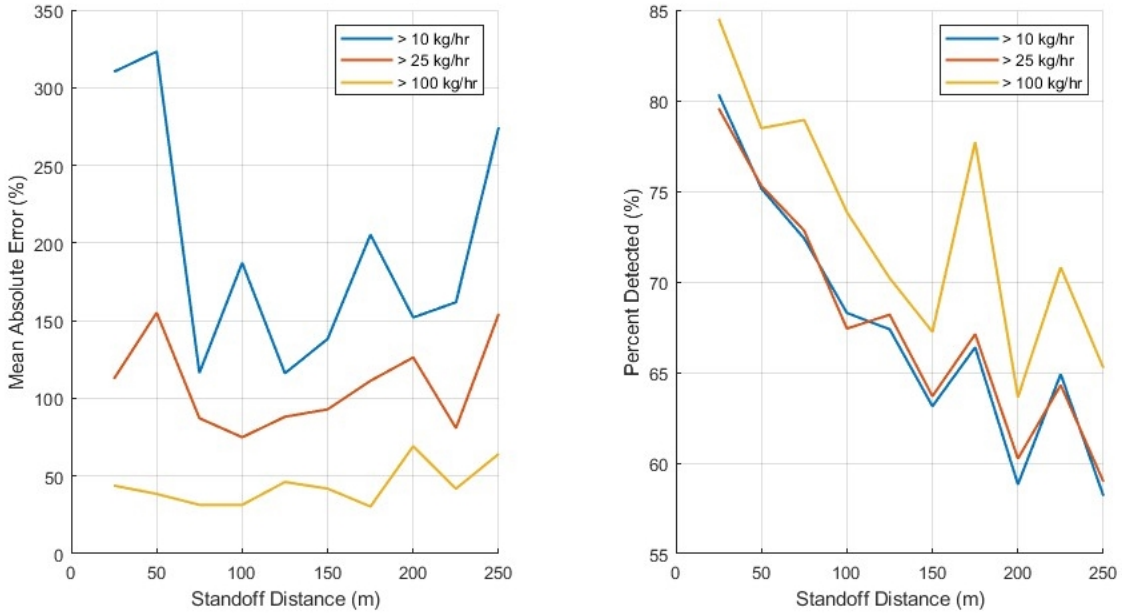

Figure 30: Standoff distance sensitivity analysis performed for a network of sensors with a measurement accuracy of 200 ppbv. (Left)The mean absolute error of the source attribution algorithm derived emission rate vs. sensor density for different emission rate magnitudes. (Right) The percent of sources detected vs. Sensor Density for different source magnitudes.

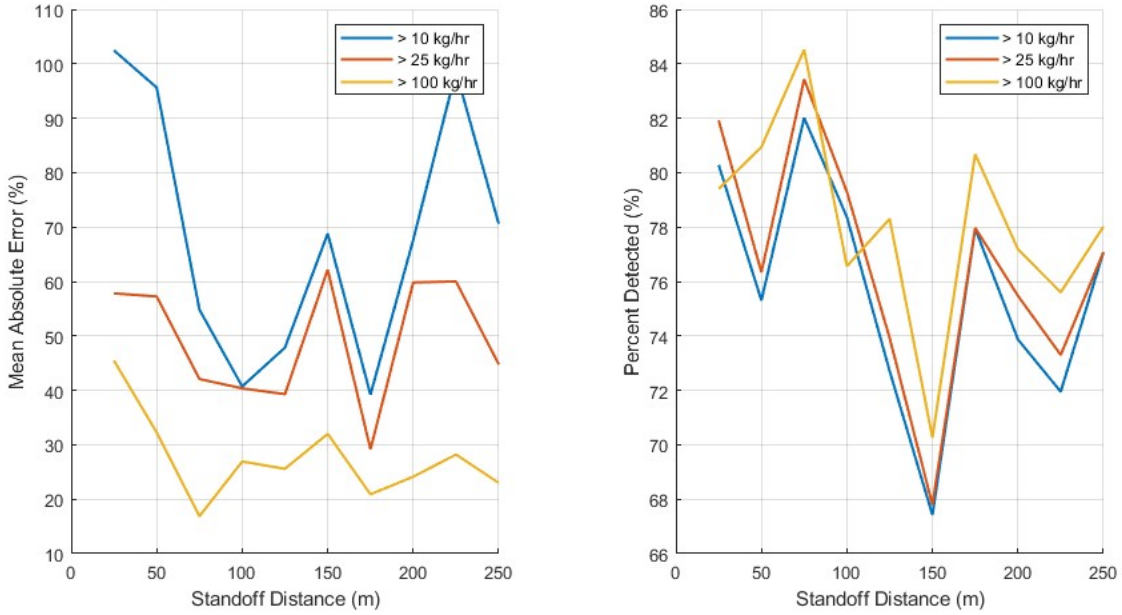

Figure 31: Standoff distance sensitivity analysis performed for a network of sensors with a measurement accuracy of 0.22 ppbv. (Left)The mean absolute error of the source attribution algorithm derived emission rate vs. sensor density for different emission rate magnitudes. (Right) The percent of sources detected vs. Sensor Density for different source magnitudes.

5. BIOGENIC MODELING OF METHANE FLUX

In the Bayesian inverse analyses conducted previously, the background methane concentration is assumed *known* for the algorithm to be able to learn emission rates and their uncertainties. In general, however, quantifying background methane concentrations can be challenging. To emphasize this, the Bayesian inverse framework can neither run nor start without a good initial estimate for background methane, which is used when determining tiered observations from the underlying concentration fields. Even when given a good initial estimate, background methane has an informative (flat) prior, which reflects its unknown value equipped with large a priori uncertainty. To illustrate the difference between knowing the background concentrations *with good confidence* vs *with poor confidence,* we rerun the inverse Bayesian framework described in Section 4.3 with a known measurement of background (spiked, certain prior) vs a good initial measurement with a flat (highly uncertain) prior, as shown in Figure 32.

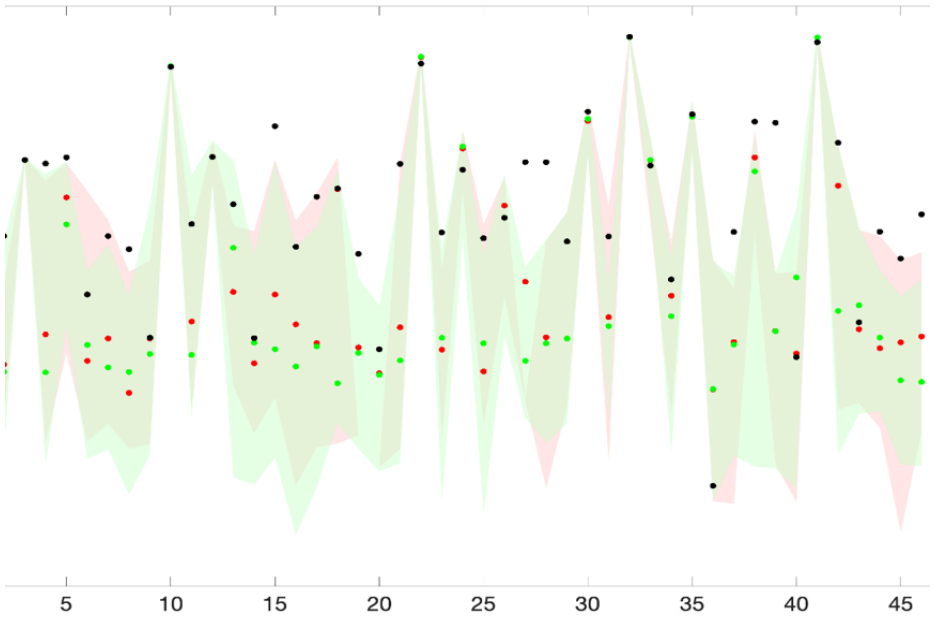

Figure 32: Uncertainty quantification of emission rates from inverse Bayesian framework between model with background (known with high confidence): estimates (red, circle) and uncertainties (red, shaded); and model with background (known with low confidence): estimates (green, circle) and uncertainties (green, shaded). True emission rates in black (circles).

Since the algorithm requires a good initial estimate to run, the estimates between both look largely similar. However, it is seen that where neither model performs well (e.g., for sources 1, 5, 7, 17, 27),

the model which assumes a known background rate with good uncertainty is more accurate at recovering the emission rates, and whose uncertainty bounds indicate a higher degree of confidence that the underlying rate is higher than estimated. For other examples (e.g., for sources 2, 9, 11, 16, 25, 38), the uncertainty bounds are much wider under the model which assumes background with poor uncertainty, and which does not typically cover the true emission rates with 95% credibility. In general, these observations emphasize the need to model and estimate background methane (i.e., coming from non O&G emissions) as accurately as possible to a) increase the accuracy of integrated methane monitoring for leak detection and b) constrain/lower the uncertainty thresholds of emission rates coming from observed O&G sources.

Monitoring and predicting methane emissions from varied sources is an emerging challenge in the global biosphere-atmosphere flux community, the success of which will have significant impacts on our ability to constrain associated uncertainty and propose steps to mitigate runaway climatic change. Methane is produced through both biogenic (natural) and anthropogenic (human-caused) sources, and any attempts to characterize methane remotely cannot inherently discriminate between the two sources. However, biogenic and anthropogenic mechanisms of methane fluxes have very different abiotic drivers, with substantially variable responses to future climate and policy intervention efforts. For instance, biogenic methane fluxes are ecotype-dependent and are controlled to varying degrees by surface temperature, moisture content, precipitation, leaf area index, lateral subsurface fluxes, organic matter composition, and soil physical properties, among other factors.

Anthropogenic sources of methane flux are dominated by O&G infrastructure, with complex and poorly constrained understanding of how methane emissions from O&G vary as a function of atmospheric conditions, and hardware state variables (e.g., component type, time since installation, time since maintenance, etc.). Current bottom-up modeling approaches subsume these mechanistic relationships using emissions factors, and scaling spatially as a function of component composition, results in massive and poorly constrained uncertainties that are static with respect to climate.

Our proposed network structure described in previous sections aims to characterize regional methane fluxes using a combination of models and measurements. Critically however, the modeling components developed herein, and generally leveraged for these efforts, are strictly focused on anthropogenic emissions from O&G infrastructure, yet this poses a known disparity between our models and measurements, given our measurements will inherently incorporate biogenic fluxes as well. If we ignore biogenic fluxes entirely, the resulting model estimates will have a minimum error term proportional to the biogenic activity. This may be a sufficient result in certain geographic areas like the Permian basin, however with increasing latitude, or for specific geographic regions prone to methane production or consumption, subsuming the biogenic processes into an error term will reduce the signal to noise potential of the system. Finally, as climate continues to change, the need to consider ecosystem physiologic interactions with non-stationary climate will continue to grow.

The biogenic flux research proposed here would directly contribute to improved estimates and scaling of biogenic and anthropogenic fluxes, through direct observations made using eddy covariance. Methane flux measurements collected across networks of eddy covariance flux tower sites are a massively underleveraged source of direct ground-atmosphere fluxes of methane that can be described as a function of biogenic and anthropogenic state variables, in response to changes in abiotic drivers. These methane flux response functions will play a critical role in scaling local measurements to landscape and regional scales.

Our measurement and modeling solution to disambiguating methane emissions from biogenic and anthropogenic sources with top-down measurements from satellites and aerial platforms hinges on using eddy covariance as a systems integration lens. This is a work in progress, but our current approach is to leverage a machine learning architecture called transformers to create an ecosystem embedding model for the terrestrial fluxes of carbon, water and energy in a general way, with specific inclusion of terrestrial sources of methane. This ecosystem embedding approach learns the relationship between abiotic drivers and methane flux as a function of remotely retrievable state variables of the system and any a priori descriptions such as O&G infrastructure composition, etc. By describing these state variables specifically in terms of anthropogenic parameters and biogenic parameters (e.g., vegetation type, leaf area index), we can dramatically improve our ability to generate bottom-up emissions estimates, with direct biogenic or anthropogenic source attribution. Ultimately, this capability is designed to operate in concert with our previously described space-borne and aerial gridded estimates of methane concentration and will permit the decomposition of an arbitrary grid cell into components that are due to anthropogenic and biogenic contributions.

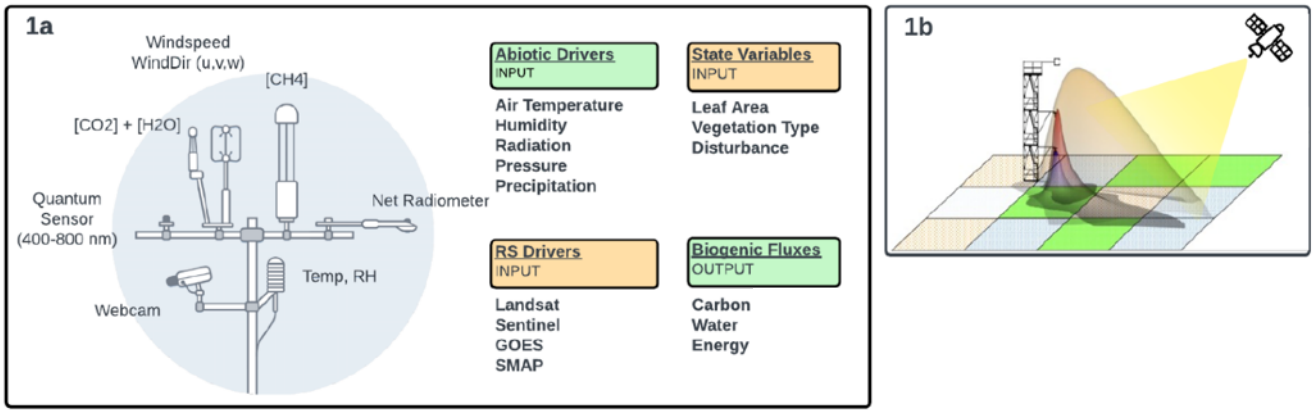

Figure 33: Conceptual framework for a measurement driven approach to modeling biogenic fluxes of carbon in a spatially and temporally heterogenous manner. Box a illustrates an example eddy covariance instrumentation tower, along with the associated data products ingested by our machine learning framework for flux modeling. Box b is a representation of the footprint model decomposition that explains the tower measurement as a spatial process that can be aligned with remote sensing (e.g., aerial and space borne) sensors.

This data driven partitioning between abiotic and biotic fluxes provides a key component to the parameterization of a biogeochemical methane production model being developed in parallel with this monitoring effort. Ultimately, our combined source specific bottom-up modeling approach will augment top-down monitoring efforts by allowing researchers to ask questions about consensus between measurements and models, and most critically, to understand how terrestrial methane production is changing as a function natural and human caused activities – a distinction that is central to managing and mitigating climate change.

6. DISCUSSION & CONCLUSION

This report details work that was conducted to create a framework that can be used to design and evaluate a multi-tiered methane sensor network to detect leaks from oil and gas industrial activities. To accomplish this objective, we first developed a steady-state gaussian plume model-based realization of methane plumes. We reviewed available sensors that could be deployed for stationary or mobile ground-based measurements, airborne measurements, or satellite measurements. We used the gaussian plume model realization to determine the detectability of individual plumes with various mobile and stationary ground-based sensors. We then conducted more robust analyses that integrated emulated sensor measurements across domains within the Permian Basin that contain multiple sources. Using several different software applications and computational techniques (e.g., Chama, inverse Bayesian modeling, and inverse gaussian plume modeling), we evaluated the ability of several integrated networks (with different associated costs) to detect sources in a timely manner and to accurately quantify emission rates of sources in the domain of interest.

While the most valuable outcome of this work is the demonstrated use of computational tools to perform source attribution and to evaluate the performance of sensor networks, the analyses we conducted yielded some useful insights:

- There is a high potential detectability of leaks in the Permian Basin from road-based mobile sources (>95% for sources with an emission rate > 10 kg/hr) that should be leveraged in future computational analyses of optimal sensor placement and monitoring assessments.
- Optimally placed (<100 m from facilities) low-cost stationary ground-based sensors can be used to achieve good detection and source attribution performance (>75% detection and < 50% mean absolute emission rate error for sources with emission rates >100 kg/hr). If desired, the deployment of strategically placed high-cost sensors can be used to enhance the performance of sensor networks.
- We estimate that total capital cost to deploy a Tier 3 sensor network with comprehensive coverage across the Permian Basin would range between $4.2-13.5 billion (to accurately cover realistic – high emissions as described by the whole Permian's source per km^2 density).

Additional repair, maintenance and calibration costs would be needed for continual monitoring over multiple years of deployment.

- Creating a fully tiered monitoring framework based upon the integration of methane sensors deployed from Tiers 1 and 2 within an optimized Tier 3 network, would provide enhanced monitoring and inverse quantification (source attribution) capabilities for rapid detection of medium— and high—level (i.e., super emitting) leaks across larger spatial areas, as exemplified over the Permian.

It should be noted that there are several factors that were not incorporated into this analysis. We assumed that we knew the locations of all potential sources based on well and facility locations reported in publicly available datasets. While this notably omits any non-oil and gas sources, the emphasis we placed on accurately quantifying background methane concentrations remains indispensable for understanding and reducing uncertainties of methane emissions from other sources. Further, the algorithms cannot yet be used in an agnostic fashion to successfully detect and attribute emissions to sources when their location is unknown. Some initial work was done to investigate this capability based on work adapted form[62], but no solution could be determined that was both accurate and computationally inexpensive. With additional effort that may leverage Sandia's expertise in developing state-of-the-art Machine Learning/Artificial Intelligence (ML/AI) algorithms deployable on High Performance Computing (HPC) systems, we are optimistic, however, that this capability can be matured to an operational state.

Lastly, a discussion regarding the funding source(s) and implementation of the sensor networks is motivated by the significant costs projected in this report. While the current regulatory climate in the United States continues to be favorable toward efforts to curb methane emissions, the implementation of an integrated sensing network is much more aggressive than even the newly established monitoring requirements under NSPS OOOOb which maintains the status quo manual and intermittent monitoring of methane sources in the Oil and Gas industry. Further, while an integrated continuous monitoring network would provide radically increased detection of methane leaks, the estimated initial capital investment of $4 billion to $7 billion to outfit the entire Permian basin is significant, but not incomprehensible when compared to $181 billion GDP generated by the oil and gas industry in 2022 or

the approximately $25 billion in 2022 tax revenue associated with Permian Basin oil and gas production activities[63].

To provide additional context, the EPA estimates that the nationwide implementation of the new NSPS OOOOb rule will cost $13 billion in initial capital costs and $1.5 billion per year in operating and maintenance costs[64]. Given that 40% and 15% [65] of domestic oil and natural gas, respectively, is produced in the Permian Basin, the estimated capital cost for a prospective monitoring network is roughly within same order of magnitude of the approximate costs that operator will incur under the new NSPS OOOOb rule (though we do not speculate that operators will be burdened with the entire cost of a methane monitoring network).

We further note that LDAR programs that are promulgated under existing and new regulations to detect and mitigate emissions often require tedious manual labor and reporting requirements that impose significant costs on operators. An automated sensing network would not pose these costs especially if the sensors implemented are low cost and do not require frequent or arduous maintenance and calibration.

REFERENCES

[1] Myhre, G.; Shindell, D.; Bréon, F.-M.; Collins, W.; Fuglestvedt, J.; Huang, J.; Koch, D.; Lamarque, J.-F.; Lee, D.; Mendoza, B.; et al. 2013: Anthropogenic and Natural Radiative Forcing. In *Climate Change 2013: The physical science basis. contribution of working group I to the fifth assessment report of IPCC the intergovernmental panel on climate change*, Stocker, T. F., Qin, D., Plattner, G.-K., Tignor, M. M., Allen, S. K., Boschung, J., Nauels, A., Xia, Y., Bex, V., Midgley, P. M. Eds.; Cambridge University Press, 2014.

[2] Masson-Delmotte, V.; Intergovernmental Panel on Climate, C. Global warming of 1.5°c : An IPCC Special Report on impacts of global warming of 1.5°c above pre-industrial levels and related global greenhouse gas emission pathways, in the contex of strengthening the global response to the thereat of blimate change, sustainable development, and efforts to eradicate poverty; Cambridge University Press, 2022.

[3] IEA(2022). *Global Methane Tracker 2022, IEA, Paris*. IEA, Paris https://www.iea.org/reports/global-methane-tracker-2022, License: CC BY 4.0 (accessed.

[4] UN. *Causes and Effects of Climate Change*. https://www.un.org/en/climatechange/science/causes-effects-climate-change (accessed 2024 1/17/2024).

[5] Etminan, M.; Myhre, G.; Highwood, E. J.; Shine, K. P. Radiative forcing of carbon dioxide, methane, and nitrous oxide: A significant revision of the methane radiative forcing. *Geophysical Research Letters* **2016**, *43* (24), 12,614-612,623.

[6] Masson-Delmotte, V. *Global warming of 1.5° c: An IPCC Special Report on impacts of global warming of 1.5° c above pre-industrial levels and related global greenhouse gas emission pathways, in the contex of strengthening the global response to the thereat of blimate change, sustainable development, and efforts to eradicate poverty*; 2018.

[7] IEA(2023). *Global Methane Tracker 2023, IEA, Paris*. IEA, Paris https://www.iea.org/reports/global-methane-tracker-2023, License: CC BY 4.0 (accessed.

[8] IEA. *Sources of methane emissions, 2021, IEA, Paris*. IEA, Paris https://www.iea.org/data-and-statistics/charts/sources-of-methane-emissions-2021, IEA. Licence: CC BY 4.0 (accessed.

[9] Aldhafeeri, T.; Tran, M.-K.; Vrolyk, R.; Pope, M.; Fowler, M. A review of methane gas detection sensors: Recent developments and future perspectives. *Inventions* **2020**, *5* (3), 28.

[10] The_White_House_Office_of_Domestic_Climate_Policy. *U.S. METHANE EMISSIONS REDUCTION ACTION PLAN: CRITICAL AND COMMONSENSE STEPS TO CUT POLLUTION AND CONSUMER COSTS, WHILE BOOSTING GOOD-PAYING JOBS AND AMERICAN COMPETITIVENESS*. The White House Office of Domestic Climate Policy 2021. https://www.whitehouse.gov/wp-content/uploads/2021/11/US-Methane-Emissions-Reduction-Action-Plan-1.pdf (accessed.

[11] QGIS. *A Free and Open Source Geographic Information System*. https://qgis.org/en/site/, CC BY-SA (accessed.

[12] Cusworth, D. H.; Thorpe, A. K.; Ayasse, A. K.; Stepp, D.; Heckler, J.; Asner, G. P.; Miller, C. E.; Yadav, V.; Chapman, J. W.; Eastwood, M. L. Strong methane point sources contribute a

disproportionate fraction of total emissions across multiple basins in the United States. *Proceedings of the National Academy of Sciences* **2022**, *119* (38), e2202338119.

[13] *Railroad Commission of Texas' statewide well database*. Railroad Commission of Texas, https://www.rrc.texas.gov/resource-center/research/data-sets-available-for-download/ (accessed.

[14] *Census Mapping Files* United States Census Bureau, https://www.census.gov/geographies/mapping-files.html (accessed 2023.

[15] Sa, I.; Corke, P. Vertical infrastructure inspection using a quadcopter and shared autonomy control. In *Field and Service Robotics: Results of the 8th International Conference*, 2014; Springer: pp 219-232.

[16] *Believer Drone Ready To Fly v2.2*. UAV Systems International https://uavsystemsinternational.com/products/believer-drone (accessed.

[17] *Mighty Fly*. https://mightyfly.com/ (accessed.

[18] *Inspire-2*. DJI, https://www.dji.com/inspire-2 (accessed 2023.

[19] *Camcopter S-100*. Schiebel, https://schiebel.net/products/camcopter-s-100/ (accessed.

[20] Kiemle, C.; Kawa, S. R.; Quatrevalet, M.; Browell, E. V. Performance simulations for a spaceborne methane lidar mission. *Journal of Geophysical Research: Atmospheres* **2014**, *119* (7), 4365-4379.

[21] Ehret, G.; Bousquet, P.; Pierangelo, C.; Alpers, M.; Millet, B.; Abshire, J. B.; Bovensmann, H.; Burrows, J. P.; Chevallier, F.; Ciais, P. MERLIN: A French-German space lidar mission dedicated to atmospheric methane. *Remote Sensing* **2017**, *9* (10), 1052.

[22] Sierk, B.; Fernandez, V.; Bézy, J.-L.; Meijer, Y.; Durand, Y.; Courrèges-Lacoste, G. B.; Pachot, C.; Löscher, A.; Nett, H.; Minoglou, K. The Copernicus CO2M mission for monitoring anthropogenic carbon dioxide emissions from space. In *International Conference on Space Optics—ICSO 2020*, 2021; SPIE: Vol. 11852, pp 1563-1580.

[23] Krebs, G. D. *Gunter's Space Page*. https://space.skyrocket.de/doc_sdat/fy-3.htm (accessed September 2022).

[24] Crisp, D.; Meijer, Y.; Munro, R.; Bowman, K.; Chatterjee, A. *A constellation architecture for monitoring carbon dioxide and methane from space, CEOS Atmospheric Composition Virtual Constellation Greenhouse Gas Team, Jet Propulsion Laboratory*; 2018.

[25] Butz, A.; Orphal, J.; Checa-Garcia, R.; Friedl-Vallon, F.; Von Clarmann, T.; Bovensmann, H.; Hasekamp, O.; Landgraf, J.; Knigge, T.; Weise, D. Geostationary Emission Explorer for Europe (G3E): mission concept and initial performance assessment. *Atmospheric Measurement Techniques* **2015**, *8* (11), 4719-4734.

[26] Chen, L.; Letu, H.; Fan, M.; Shang, H.; Tao, J.; Wu, L.; Zhang, Y.; Yu, C.; Gu, J.; Zhang, N. An introduction to the Chinese high-resolution Earth observation system: Gaofen-1~ 7 civilian satellites. *Journal of Remote Sensing* **2022**.

[27] Zou, M. GaoFen-5 GHG Monitoring Instrument. In *CEOS-AC-VC-14th*, College Park, MD, 2-4 May, 2018, 2018.

[28] Fishman, J.; Iraci, L. T.; Al-Saadi, J.; Chance, K.; Chavez, F.; Chin, M.; Coble, P.; Davis, C.; DiGiacomo, P.; Edwards, D. The United States' next generation of atmospheric composition and coastal ecosystem measurements: NASA's Geostationary Coastal and Air Pollution Events (GEO-CAPE) mission. *Bulletin of the American Meteorological Society* **2012**, *93* (10), 1547-1566.

[29] Sheng, J.-X.; Jacob, D. J.; Maasakkers, J. D.; Zhang, Y.; Sulprizio, M. P. Comparative analysis of low-Earth orbit (TROPOMI) and geostationary (GeoCARB, GEO-CAPE) satellite instruments for constraining methane emissions on fine regional scales: application to the Southeast US. **2018**.

[30] Al-Saadi, J.; Chin, M.; da Silva, A.; Edwards, D.; Frost, G.; Henze, D.; Iraci, L.; Jacob, D.; Mannino, A.; Natraj, V. Advancing the Science of Both Coastal Ocean Biophysics and Atmospheric Pollution Chemistry: A Final Report to the Nasa Earth Science Division by the GEO-CAPE Team. **2018**.

[31] Moore III, B.; Crowell, S. M.; Rayner, P. J.; Kumer, J.; O'Dell, C. W.; O'Brien, D.; Utembe, S.; Polonsky, I.; Schimel, D.; Lemen, J. The potential of the Geostationary Carbon Cycle Observatory (GeoCarb) to provide multi-scale constraints on the carbon cycle in the Americas. *Frontiers in Environmental Science* **2018**, *6*, 109.

[32] Polonsky, I.; O'Brien, D.; Kumer, J.; O'Dell, C. Performance of a geostationary mission, geoCARB, to measure CO 2, CH 4 and CO column-averaged concentrations. *Atmospheric Measurement Techniques* **2014**, *7* (4), 959-981.

[33] NASA.

[34] *Geostationary Carbon Cycle Observatory at the University of Oklahoma*. https://www.ou.edu/geocarb (accessed.

[35] Xi, X.; Natraj, V.; Shia, R.-L.; Luo, M.; Zhang, Q.; Newman, S.; Sander, S.; Yung, Y. Simulated retrievals for the remote sensing of CO 2, CH 4, CO, and H 2 O from geostationary orbit. *Atmospheric Measurement Techniques* **2015**, *8* (11), 4817-4830.

[36] Kuze, A.; Suto, H.; Shiomi, K.; Kawakami, S.; Tanaka, M.; Ueda, Y.; Deguchi, A.; Yoshida, J.; Yamamoto, Y.; Kataoka, F. Update on GOSAT TANSO-FTS performance, operations, and data products after more than 6 years in space. *Atmospheric Measurement Techniques* **2016**, *9* (6), 2445-2461.

[37] Parker, R. J.; Webb, A.; Boesch, H.; Somkuti, P.; Barrio Guillo, R.; Di Noia, A.; Kalaitzi, N.; Anand, J. S.; Bergamaschi, P.; Chevallier, F. A decade of GOSAT Proxy satellite CH< sub> 4</sub> observations. *Earth System Science Data* **2020**, *12* (4), 3383-3412.

[38] Glumb, R.; Davis, G.; Lietzke, C. The TANSO-FTS-2 instrument for the GOSAT-2 greenhouse gas monitoring mission. In *2014 IEEE Geoscience and Remote Sensing Symposium*, 2014; IEEE: pp 1238-1240.

[39] Staebell, C.; Sun, K.; Samra, J.; Franklin, J.; Chan Miller, C.; Liu, X.; Conway, E.; Chance, K.; Milligan, S.; Wofsy, S. Spectral calibration of the MethaneAIR instrument. *Atmospheric Measurement Techniques* **2021**, *14* (5), 3737-3753.

[40] Chan Miller, C.; Roche, S.; Wilzewksi, J. S.; Liu, X.; Chance, K.; Souri, A. H.; Conway, E.; Luo, B.; Samra, J.; Hawthorne, J. Methane retrieval from MethaneAIR using the CO 2 Proxy

Approach: A demonstration for the upcoming MethaneSAT mission. *EGUsphere* **2023**, *2023*, 1-40.

[41] Sentinel_Online. *SentiWiki*. https://sentinels.copernicus.eu/web/sentinel/home (accessed.

[42] Geyl, R.; Ruch, E.; Leplan, H.; Riguet, F.; Lopez, S. Precision space freeform optics for Microcarb. In *Optical Manufacturing and Testing XIII*, 2020; SPIE: Vol. 11487, pp 170-178.

[43] Lachance, R. L.; McConnell, J. C.; McElroy, C. T.; O'Neill, N.; Nassar, R.; Buijs, H.; Rahnama, P.; Walker, K.; Martin, R.; Sioris, C. PCW/PHEOS-WCA: quasi-geostationary Arctic measurements for weather, climate, and air quality from highly eccentric orbits. In *Sensors, Systems, and Next-Generation Satellites XVI*, 2012; SPIE: Vol. 8533, pp 163-172.

[44] Nassar, R. The Potential for Arctic and Boreal CO and CH4 Observations from a Highly Eliptical Orbit (HEO) Mission. In *CEOS AC-VC*, Paris, France, 2017; CNES, Ed.

[45] Frankenberg, C.; Meirink, J. F.; Bergamaschi, P.; Goede, A.; Heimann, M.; Körner, S.; Platt, U.; van Weele, M.; Wagner, T. Satellite chartography of atmospheric methane from SCIAMACHY on board ENVISAT: Analysis of the years 2003 and 2004. *Journal of Geophysical Research: Atmospheres* **2006**, *111* (D7).

[46] Butz, A.; Galli, A.; Hasekamp, O.; Landgraf, J.; Tol, P.; Aben, I. TROPOMI aboard Sentinel-5 Precursor: Prospective performance of CH4 retrievals for aerosol and cirrus loaded atmospheres. *Remote sensing of environment* **2012**, *120*, 267-276.

[47] Lorente, A.; Borsdorff, T.; Butz, A.; Hasekamp, O.; Schneider, A.; Wu, L.; Hase, F.; Kivi, R.; Wunch, D.; Pollard, D. F. Methane retrieved from TROPOMI: improvement of the data product and validation of the first 2 years of measurements. *Atmospheric Measurement Techniques* **2021**, *14* (1), 665-684.

[48] Lauvaux, T.; Giron, C.; Mazzolini, M.; d'Aspremont, A.; Duren, R.; Cusworth, D.; Shindell, D.; Ciais, P. Global assessment of oil and gas methane ultra-emitters. *Science* **2022**, *375* (6580), 557-561.

[49] Clerbaux, C.; Hadji-Lazaro, J.; Turquety, S.; Mégie, G.; Coheur, P.-F. Trace gas measurements from infrared satellite for chemistry and climate applications. *Atmospheric Chemistry and Physics* **2003**, *3* (5), 1495-1508.

[50] Xiong, X.; Barnet, C.; Maddy, E.; Sweeney, C.; Liu, X.; Zhou, L.; Goldberg, M. Characterization and validation of methane products from the Atmospheric Infrared Sounder (AIRS). *Journal of Geophysical Research: Biogeosciences* **2008**, *113* (G3).

[51] NASA. *AIRS: Atmospheric Infrared Sounder* https://airs.jpl.nasa.gov/ (accessed 2023.

[52] Worden, J.; Kulawik, S.; Frankenberg, C.; Payne, V.; Bowman, K.; Cady-Pereira, K.; Wecht, K.; Lee, J.; Noone, D. Profiles of CH4, HDO, H2O, and N2O with improved lower tropospheric vertical resolution from Aura TES radiances. *Atmospheric Measurement Techniques Discussions* **2012**, *4* (6), 6679-6721.

[53] Wecht, K. J.; Jacob, D. J.; Wofsy, S. C.; Kort, E.; Worden, J.; Kulawik, S.; Henze, D.; Kopacz, M.; Payne, V. Validation of TES methane with HIPPO aircraft observations: implications for inverse modeling of methane sources. *Atmospheric Chemistry and Physics* **2012**, *12* (4), 1823-1832.

[54] Gambacorta, A.; Barnet, C. D.; Smith, N.; Pierce, R. B.; Smith, J. W.; Spackman, J. R.; Goldberg, M. The NPP and J1 NOAA Unique Combined Atmospheric Processing System (NUCAPS) for atmospheric thermal sounding: recent algorithm enhancements tailored to near real time users applications. In *AGU Fall Meeting Abstracts*, 2016; Vol. 2016, pp IN33D-07.

[55] L3Harris. *Cross-Track Infrared Sounder*. https://www.l3harris.com/all-capabilities/cross-track-infrared-sounder-cris (accessed 2022 November).

[56] Klise, K. A.; Nicholson, B. L.; Laird, C. D. *Sensor placement optimization using Chama*; Sandia National Lab.(SNL-NM), Albuquerque, NM (United States), 2017.

[57] Mohan, M.; Siddiqui, T. Analysis of various schemes for the estimation of atmospheric stability classification. *Atmospheric environment* **1998**, *32* (21), 3775-3781.

[58] NOAA_Air_Resource_Laboratory. *Pasquill Stability Classes*. NOAA, 2023. www.ready.noaa.gov/READYpgclass.php (accessed 2023 December).

[59] Ravikumar, A. P.; Wang, J.; Brandt, A. R. Are optical gas imaging technologies effective for methane leak detection? *Environmental science & technology* **2017**, *51* (1), 718-724.

[60] Weidmann, D.; Hirst, B.; Jones, M.; Ijzermans, R.; Randell, D.; Macleod, N.; Kannath, A.; Chu, J.; Dean, M. Locating and Quantifying Methane Emissions by Inverse Analysis of Path-Integrated Concentration Data Using a Markov-Chain Monte Carlo Approach. *ACS Earth and Space Chemistry* **2022**, *6* (9), 2190-2198.

[61] Rutherford, J. S.; Sherwin, E. D.; Ravikumar, A. P.; Heath, G. A.; Englander, J.; Cooley, D.; Lyon, D.; Omara, M.; Langfitt, Q.; Brandt, A. R. Closing the methane gap in US oil and natural gas production emissions inventories. *Nature communications* **2021**, *12* (1), 4715.

[62] Hwang, Y.; Kim, H. J.; Chang, W.; Yeo, K.; Kim, Y. Bayesian pollution source identification via an inverse physics model. *Computational Statistics & Data Analysis* **2019**, *134*, 76-92.

[63] Permian_Strategic_Partnership. *2022 Power of the Permian Economic Report*. 2022. https://permianpartnership.org/power-of-the-permian/ (accessed 2024 January 16).

[64] Radiation, O. o. A. a. Regulatory Impact Analysis of the Standards of Performance for New, Reconstructed, and Modified Sources and Emissions Guidelines for Existing Sources: Oil and Natural Gas Sector Climate Review. Agency, U. S. E. P., Standards, O. o. A. Q. P. a., Division, H. a. E. I., Eds.

[65] Railroad_Commission_of_Texas. *Permian Basin*. www.rrc.texas.gov/oil-and-gas/major-oil-and-gas-formations/permian-basin/#:~:text=The%20greater%20Permian%20Basin%20accounts,Federal%20Reserve%20Bank%20of%20Dallas. (accessed 2024 January).

[66] Martin, D.O., 1976. Comment On" The Change of Concentration Standard Deviations with Distance". Journal of the Air Pollution Control Association, 26(2), pp.145-147.

APPENDIX A. GIS WORKFLOW FOR MOBILE SENSOR ZOD ANALYSIS

The "Zone of Detection" for a mobile sensor is a planimetric area in the x,y plane of a methane plume where concentrations of CH_4 are above normal background concentrations. The surface on which the ZOD is projected is termed here as the Primary ZOD Surface. As the dimensions of the ZOD are in meters, we can transform the ZOD's geometry directly onto a cartographic map with geographic coordinates. The origin of the leak (0,0) becomes the origin of a local coordinate system on which the length and width of the ZOD can be plotted. The length of a ZOD swept 360° around the local origin represents a feature we term the Zone of Detection Buffer (ZODB) (Figure 34).

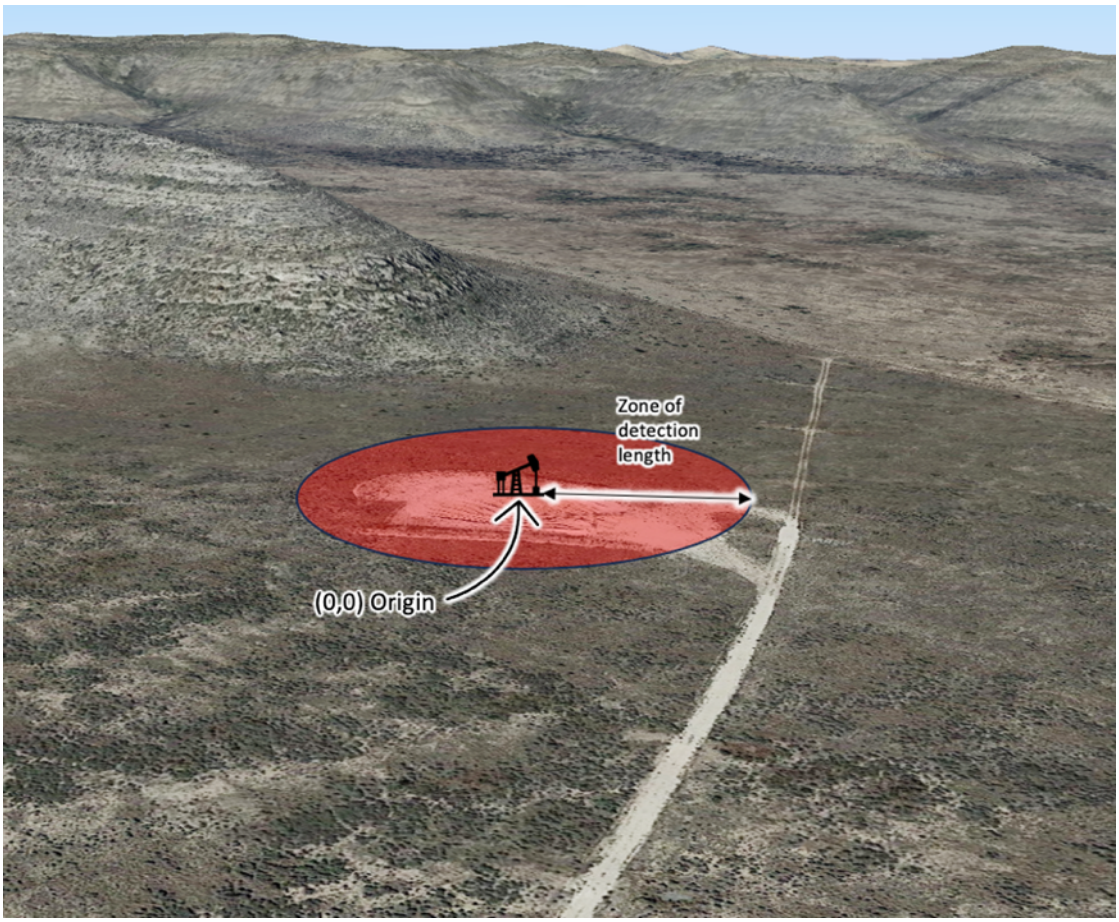

Figure 34: Example of the planimetric outline for a Zone of Detection Buffer (ZODB) around a well locations.

The ZODB represents the area within which the ZOD can possibly fall for any wind vector parallel to the Primary ZOD surface.

If the wind direction is not known, then the whole ZODB could be used as a means to estimate the boundary within which the ZOD could be located (Figure 35). A road that can support travel of the mobile sensor to the ZODB qualifies the well associated with that ZODB as monitorable.

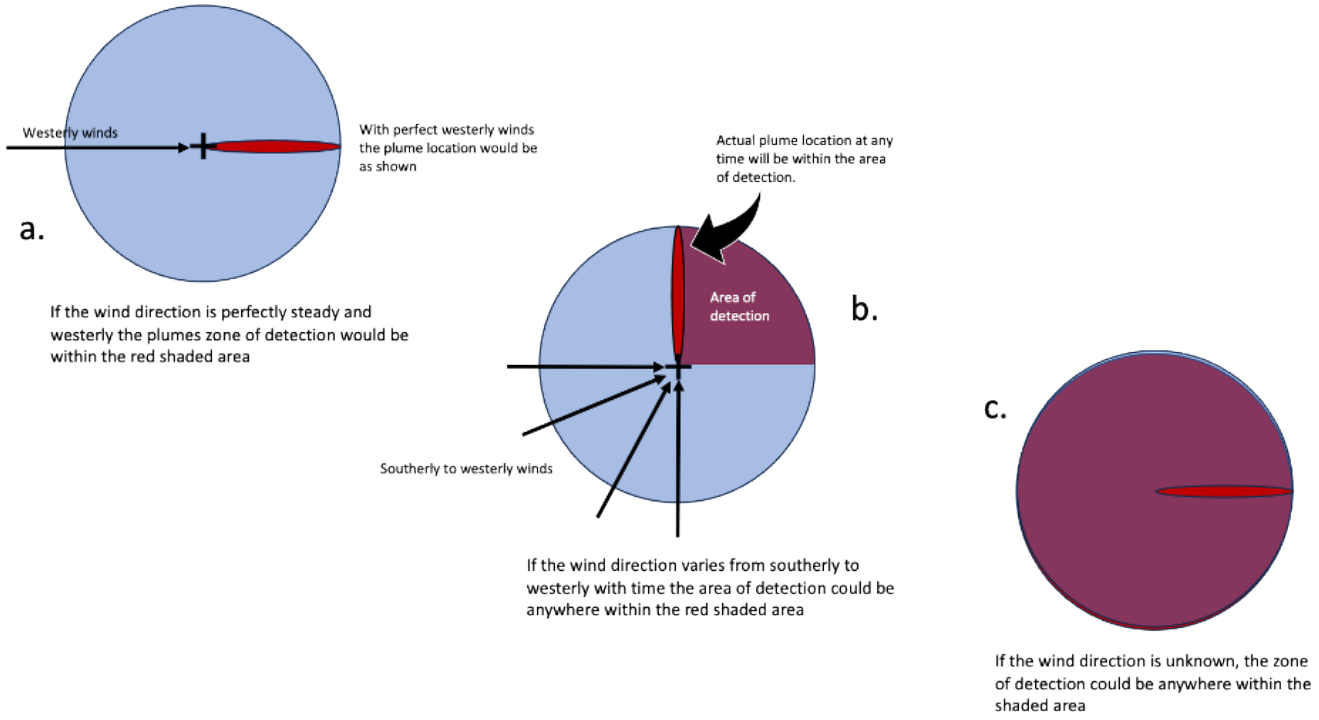

Figure 35: a) An example of the area within a circle of radius w, in the case where wind is from the west. b) If the wind direction shifts from the south to the west, the area of detection during that transition will be somewhere within the purple area. c) If the wind direction is unknown, the area of detection could be anywhere within the purple area.

A.1. Overview of Study Area and Geographic Distribution of Wells and Roads

Figure 36 is a map showing the geographic extent of the Permian Basin. Publicly accessible well and road data for this area was collected. Well data was obtained from the Railroad Commission of Texas' statewide Well database[13] and the New Mexico Energy, Minerals and Natural Resources Departments Oil Conservation Divisions Geospatial Hub[13] (Figure 37). Publicly accessible roads of the Permian

Basin from the US Census Bureau's road databases for the states of Texas and New Mexico are shown in Figure 38[14].

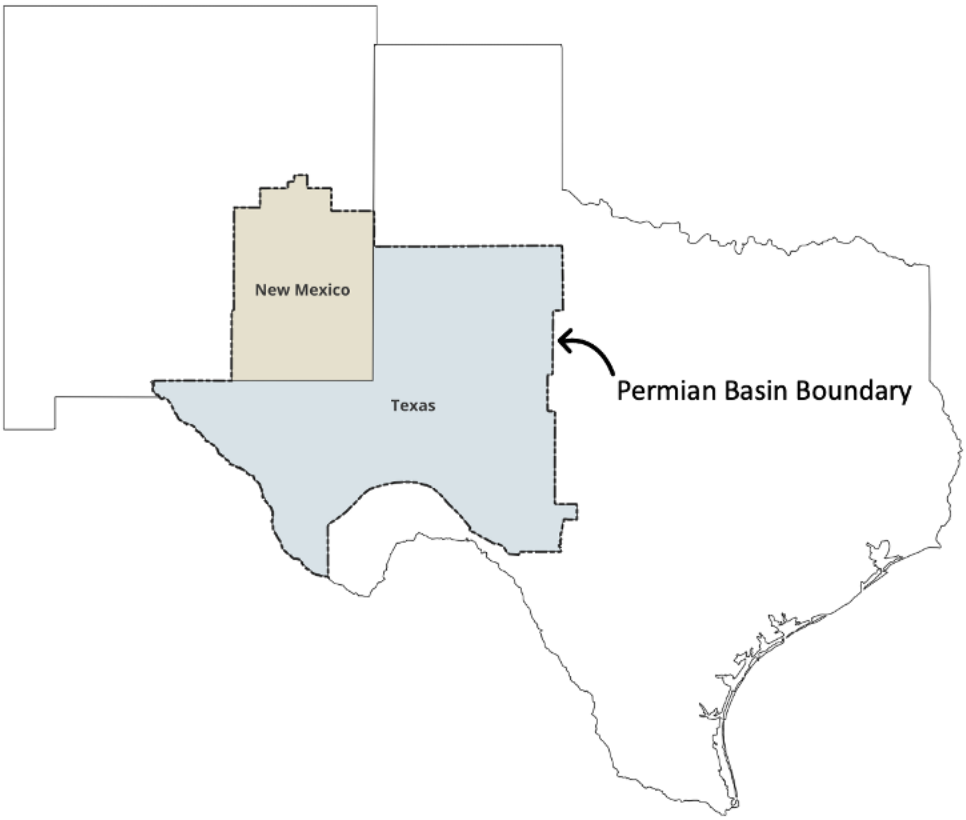

Figure 36: Location of the Permian Basin, Eastern New Mexico, and Western Texas

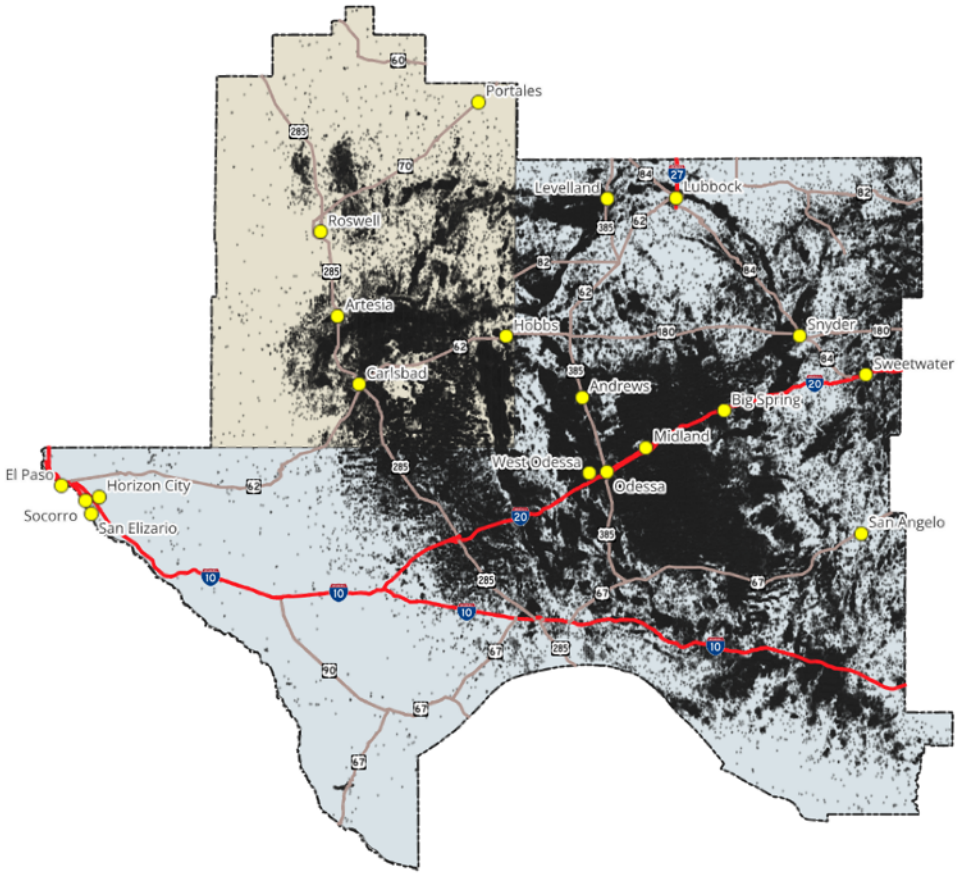

Figure 37: The Permian Basin's oil and gas wells. Major roads/cities shown for reference.

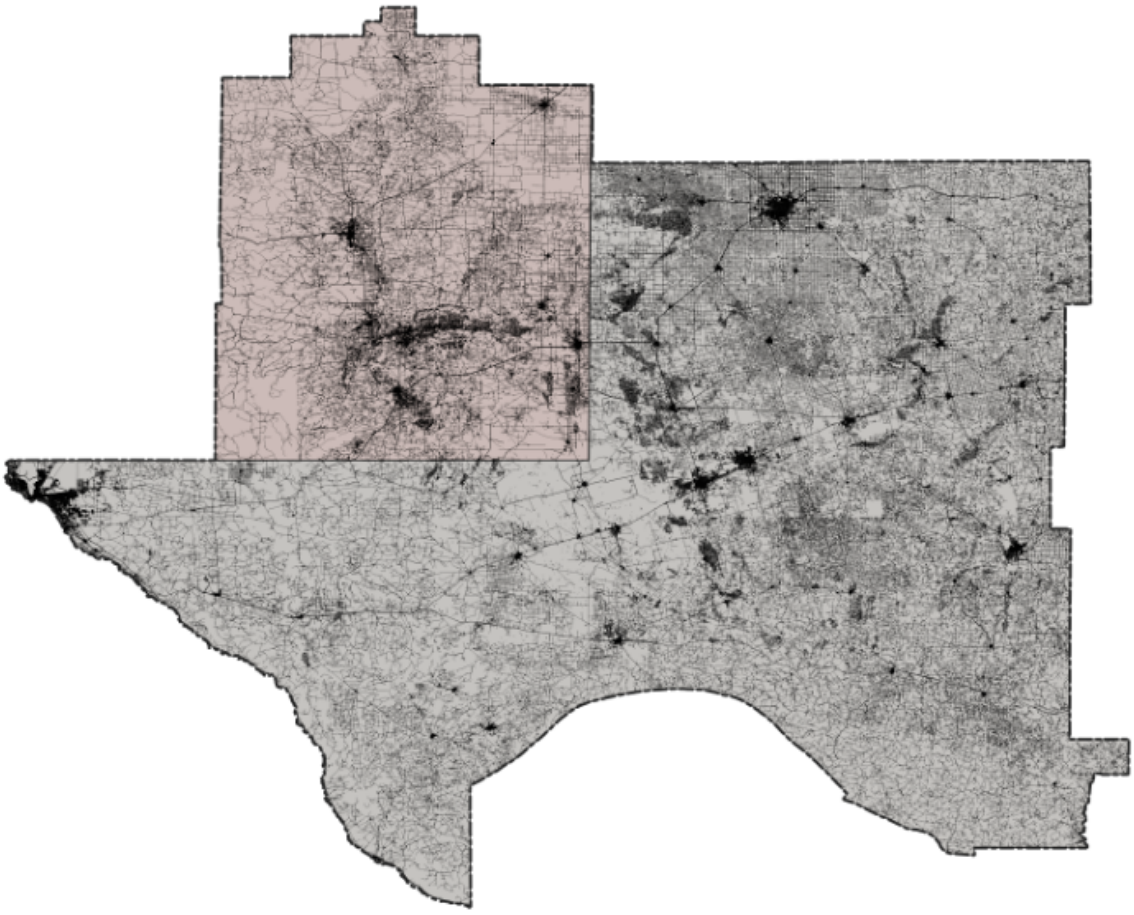

Figure 38: Publicly accessible roads of the Permian Basin.

A.2. A First-Order Approximation of Wells in the Permian Basin that are Monitorable by Tier 3 Sensors

In this section, we present a first-order approximation for the percentage of wells in the Permian Basin that are monitorable by Tier 3 sensors. A monitorable well in this case is a well whose ZODB intersects a road that is passable by a mobile sensor.

For all the wells in the database, the ZOD length was used to define the ZODB. The ZODBs evaluated were constructed from the data presented in Section 1.3 and 1.4. The result of the calculations for a variety of leak rates, wind speeds, and ZOD CH_4 concentrations allowed us to answer the following questions:

1. What is the percentage of wells in the Permian Basin that are monitorable by mobile sensors?
2. What is the total area of the Permian Basin that is within a ZODB?
3. Are there areas where monitoring wells via mobile sensor is not currently possible?

The workflow we used to determine the answers to these questions is shown in Figure 39. It was implemented as a standalone python application that leveraged the Python API of an open-source application called QGIS[11], a full featured Geographic Information System that has a mature API accessible in both C++ and Python.

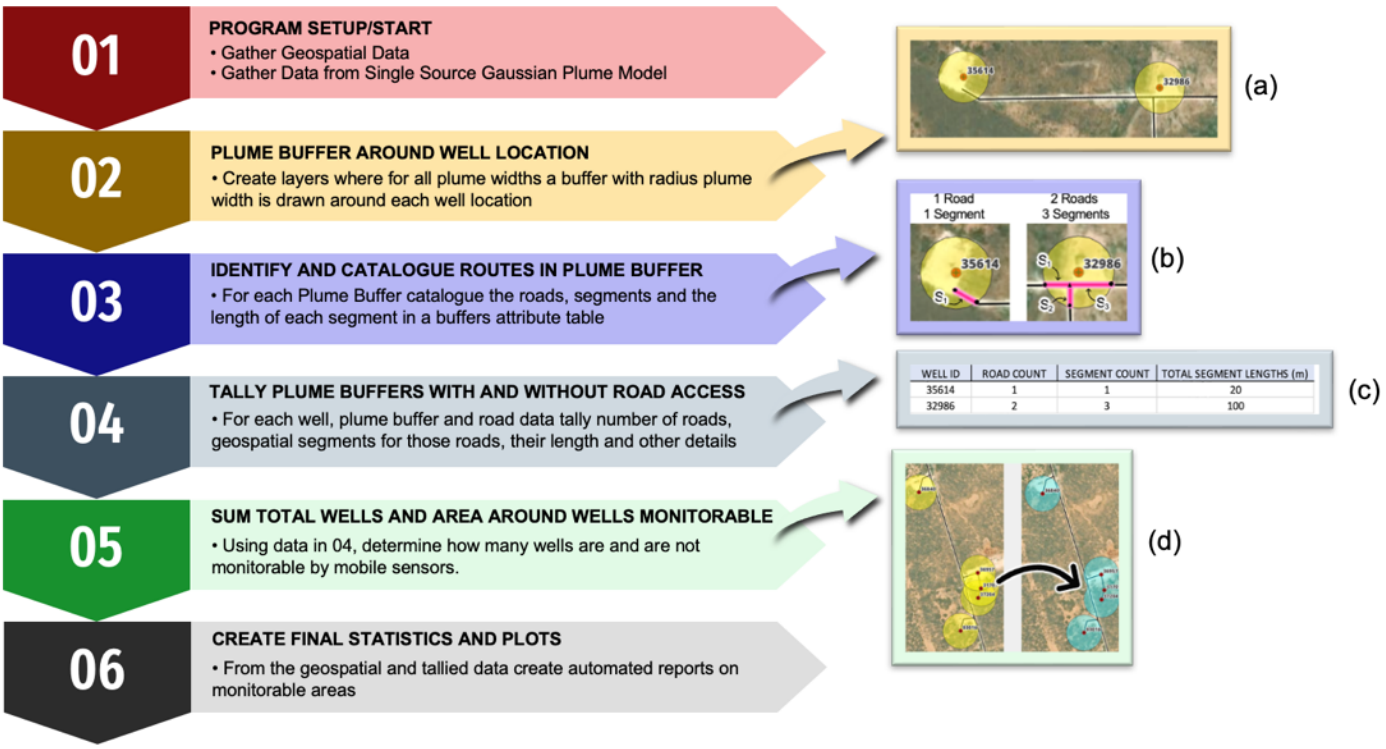

Figure 39: Analytics Workflow in analysis using QGIS

There are six steps to the workflow. The first involved the gathering of data from publicly accessible web sources and the loading of the data in Appendix A and B into a data structure accessible by the QGIS Python API.

Step 2 involves creating the ZODB for all wells at all parameters of the data in Step 1. The resulting data were output as Shapefiles that possess attribute tables storing attributes for each ZODB. This includes geographic location in latitude and longitude, area, and perimeter for of the ZODB. An example of output for this process is shown Figure 40.

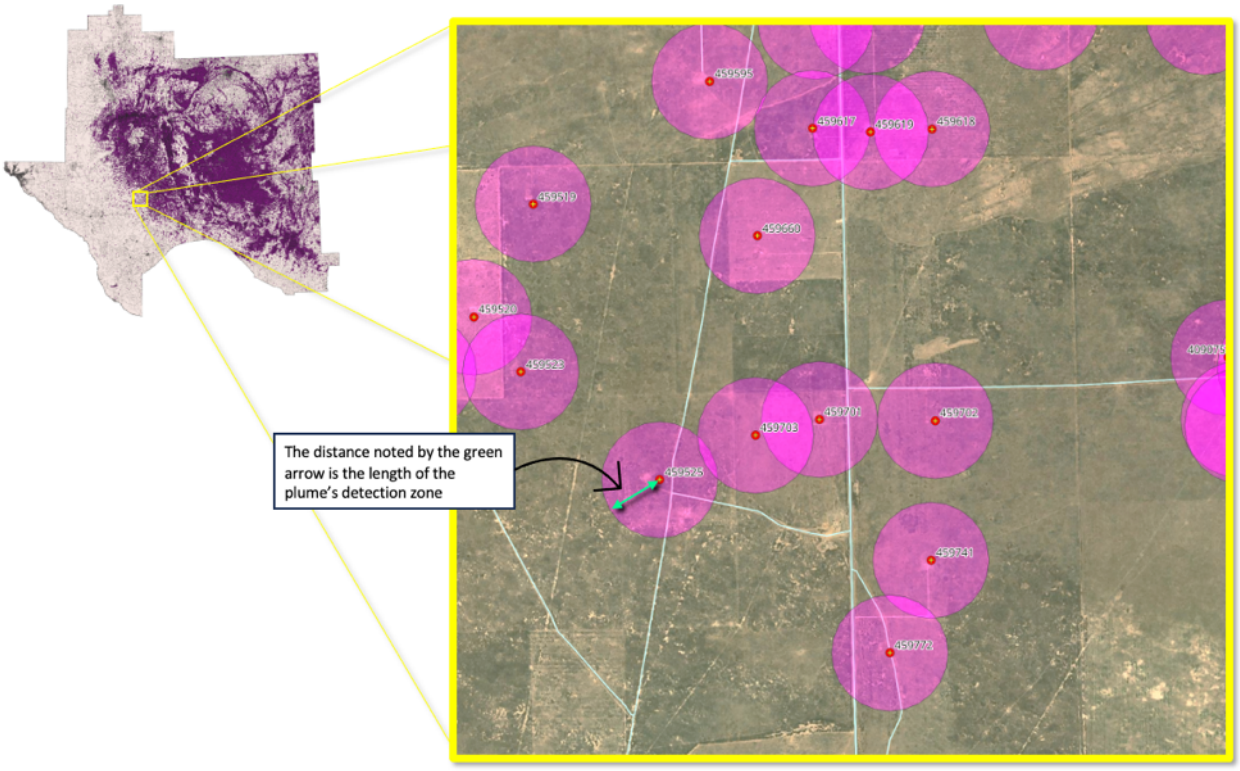

Figure 40: An example of Step 2 results. Each of the ZODBs have a radius that is the length of the plume representing the ZOD for differing wind speeds, leak rates, and background concentrations.

In step 3, we run a process that checks for intersections of ZODBs and roads. Step 4 then identifies ZODBs with one or more roads intersecting them as well as those ZODBs that intersect no roads (Figure 41).

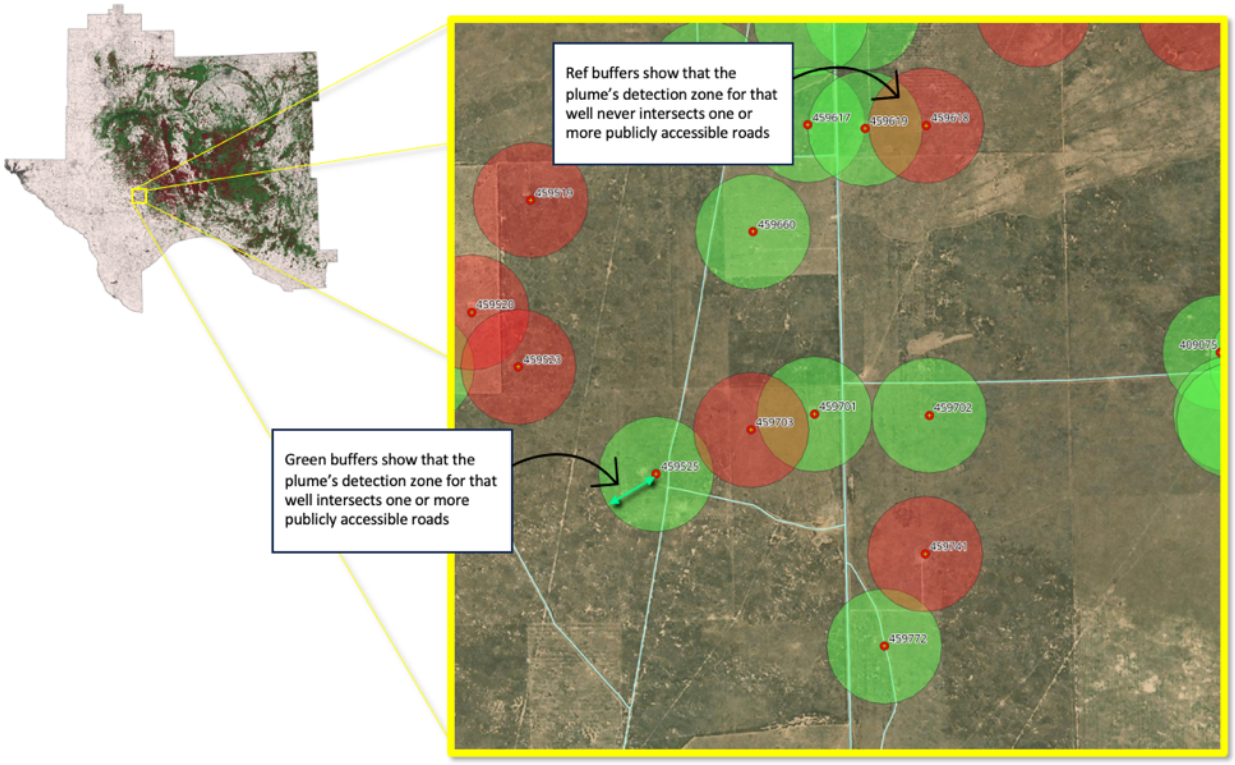

Figure 41: A map representing the output of process 3. There are two sets of items in this case, the first is all ZODBs that intersect one or more roads (Green) and those that intersect none (Red).

As we saw in the results of steps 1-4, the ZODBs can overlap in some cases. This is particularly true in situations where the length of the ZOD is large. This means that there some ZODBs that do not intersect roads but do intersect ZODBs from other wells. Even though a well's ZODB could intersect another wells ZODB, we would not count these wells as monitorable as they would not have a road intersecting them.

Step 5 involves "dissolving" the intersections and overlaps of the ZODBs for those that intersect roads. In this case the results are a multipart polygon (Figure 42). This area represents the full area (not number of wells) that is physically monitorable by ground sensors. In addition, it also defines what we term here as "dead zones" or zones where Tier 3 mobile vehicles would not be deployable. The final step of the process, step 6, is simply producing the plots, statistics, and other artifacts for this report.

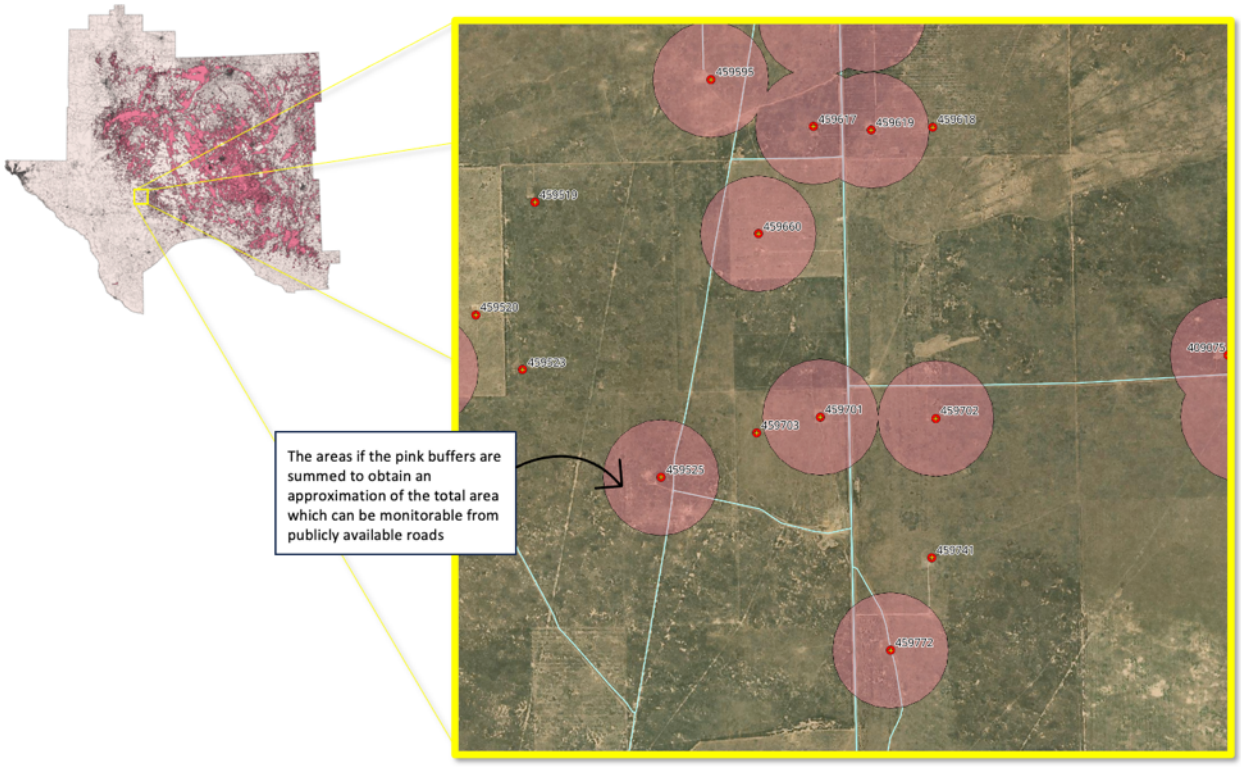

Figure 42: Step 5 is a "dissolve" step. The dissolve step aggregates all the polygons in a layer into one entity.

APPENDIX B. MONITORABLE AND DEAD ZONE AREA PERCENTAGES

		BACKGROUND CH_4	
		Wind Speed 0.01 m/s	Wind Speed 1 m/s
Leak Rate (kg/hr)	100	94.28% Monitorable with 5.72% Dead Zone	21.35% Monitorable with 78.65% Dead Zone
	10	66.09% Monitorable with 33.91% Dead Zone	No Data
	1	24.06% Monitorable with 75.94% Dead Zone	No Data

		10% Above Background CH_4	
		Wind Speed 0.01 m/s	Wind Speed 1 m/s
Leak Rate (kg/hr)	100	94.28% Monitorable with 5.72% Dead Zone	21.35% Monitorable with 78.65% Dead Zone
	10	65.91% Monitorable with 34.09% Dead Zone	No Data
	1	22.03% Monitorable with 77.97% Dead Zone	No Data

		100% Above Background CH_4	
		Wind Speed 0.01 m/s	Wind Speed 1 m/s
Leak Rate (kg/hr)	100	92.08% Monitorable with 7.92% Dead Zone	12.79% Monitorable with 87.21% Dead Zone
	10	56.23% Monitorable with 43.77% Dead Zone	No Data
	1	15.00% Monitorable with 85.00% Dead Zone	No Data

		1000% Above Background CH_4	
		Wind Speed 0.01 m/s	Wind Speed 1 m/s
Leak Rate (kg/hr)	100	27.83% Monitorable with 72.17% Dead Zone	No Data
	10	27.83% Monitorable with 72.17% Dead Zone	No Data
	1	No Data	No Data

		10000% Above Background CH_4	
		Wind Speed 0.01 m/s	Wind Speed 1 m/s
Leak Rate (kg/hr)	100	38.84% Monitorable with 61.16% Dead Zone	No Data
	10	No Data	No Data
	1	No Data	No Data

DISTRIBUTION

Email—Internal

Name	Org.	Sandia Email Address
Technical Library	1911	sanddocs@sandia.gov

Email—External (encrypt for CUI)

Name	Company Email Address	Company Name
Jared Ciferno	jared.ciferno@hq.doe.gov	DOE FECM

Hardcopy—Internal

Number of Copies	Name	Org.	Mailstop

Hardcopy—External

Number of Copies	Name	Company Name and Company Mailing Address

This page left blank

Sandia National Laboratories is a multimission laboratory managed and operated by National Technology & Engineering Solutions of Sandia LLC, a wholly owned subsidiary of Honeywell International Inc. for the U.S. Department of Energy's National Nuclear Security Administration under contract DE-NA0003525.